



HAL
open science

Micromorphic crystal plasticity approach to damage regularization and size effects in martensitic steels

Matti Lindroos, Jean-Michel Scherer, Samuel Forest, Anssi Laukkanen, Tom Andersson, Joonas Vaara, Antti Mäntylä, Tero Frondelius

► To cite this version:

Matti Lindroos, Jean-Michel Scherer, Samuel Forest, Anssi Laukkanen, Tom Andersson, et al.. Micromorphic crystal plasticity approach to damage regularization and size effects in martensitic steels. *International Journal of Plasticity*, 2022, 151, pp.103187. 10.1016/j.ijplas.2021.103187 . hal-03589992

HAL Id: hal-03589992

<https://hal.science/hal-03589992v1>

Submitted on 26 Feb 2022

HAL is a multi-disciplinary open access archive for the deposit and dissemination of scientific research documents, whether they are published or not. The documents may come from teaching and research institutions in France or abroad, or from public or private research centers.

L'archive ouverte pluridisciplinaire **HAL**, est destinée au dépôt et à la diffusion de documents scientifiques de niveau recherche, publiés ou non, émanant des établissements d'enseignement et de recherche français ou étrangers, des laboratoires publics ou privés.



Micromorphic crystal plasticity approach to damage regularization and size effects in martensitic steels

Matti Lindroos ^{a,*}, Jean-Michel Scherer ^{b,d}, Samuel Forest ^b, Anssi Laukkanen ^a, Tom Andersson ^a, Joonas Vaara ^c, Antti Mäntylä ^c, Tero Frondelius ^{c,e}

^a *Integrated Computational Materials Engineering, VTT, Espoo, Finland*

^b *MINES ParisTech, PSL University, MAT – Centre des matériaux, CNRS UMR 7633, BP 87 91003, Evry, France*

^c *R&D and Engineering, Wärtsilä, P.O. Box 244, 65101, Vaasa, Finland*

^d *Université Paris-Saclay, CEA, Service d'Étude des Matériaux Irradiés, 91191, Gif-sur-Yvette, France*

^e *University of Oulu, Erkki Koiso-Kanttilan katu 1, 90014, Oulu, Finland*

ARTICLE INFO

Keywords:

Micromorphic
Gradient plasticity
Crystal plasticity
Damage

ABSTRACT

A reduced micromorphic model is formulated in the scope of crystal plasticity and crystalline cleavage damage. The finite strain formulation utilizes a single additional microvariable that is used to regularize localized inelastic deformation mechanisms. Damage is formulated as a strain-like variable to fit the generalized micromorphic *microslip* and/or *microdamage* based formulation. Strategies of treating slip and damage simultaneously and separately as non-local variables are investigated. The model accounts for size-effects that simultaneously affect the hardening behavior and allow to predict finite width damage localization bands. The results show that the micromorphic extension introduces extra-hardening in the vicinity of grain boundaries and slip localization zones in polycrystals. At the single crystal level slip band width is regularized. Two ways of dealing with damage localization were identified: An indirect method based on controlling width of slip bands that act as initiation sites for damage and a direct method in which damage flow is regularized together with or separately from plastic slip. Application to a real martensitic steel microstructure is investigated.

1. Introduction

Martensitic steels are widely used engineering materials because of their high strength and decent ductility, that play a role, for example, in the fatigue performance of the material. The microstructure of martensite is often rationalized by making distinction of prior austenite, blocks, packets and laths (Morito et al., 2003; Chatterjee et al., 2018).

Various recent experimental and numerical studies have been devoted to investigate the deformation response of dual-phase, martensitic, and bainitic steels with an objective to reveal reasoning for strength–ductility trade-off, thermo-mechanical response, response to cyclic fatigue loading, and aging behavior of different steel grades. A matter of particular interest is the quantification of strengthening induced by plastic activity impeded by the hierarchical microstructure of these materials (Morsdorf et al., 2016; Du et al., 2016; Kwak et al., 2016). Strain heterogeneity further increases in the presence of soft ferrite phase and intra-lath greasy austenite layers, which both can notably or only marginally increase the materials ductility (Asik et al., 2020; Tasan et al., 2014; Maresca et al., 2014, 2016). The latter allows for ductile-like plastic deformation accommodation between hard laths, but can transform to martensite already at small strains (Morsdorf et al., 2016). The ferrite phase, in turn, is stable and

* Corresponding author.

E-mail address: matti.lindroos@vtt.fi (M. Lindroos).

<https://doi.org/10.1016/j.ijplas.2021.103187>

Received 6 June 2020; Received in revised form 15 December 2021

Available online 13 January 2022

0749-6419/© 2021 The Author(s). Published by Elsevier Ltd. This is an open access article under the CC BY license

(<http://creativecommons.org/licenses/by/4.0/>).

actively accommodating strains in the mixtures of ferrite–martensite–austenite microstructures, often at the expense of overall strength (Laukkanen et al., 2021). Adjusting the suitable phase fractions is challenging whenever detrimental effects are aimed to be minimized. As it comes, precipitates are one source of fine scale strengthening, however, they can also act as nucleation sites for, for example, brittle failure (Li et al., 2014; Vincent et al., 2010; Monnet et al., 2019).

Optimization of advanced steels using robust R&D processes becomes attractive to enhance their performance and sustainability efficiently. To accomplish rapid development of these materials towards desired extreme mechanical properties, a valid computational framework can be used. In aforementioned studies, crystal plasticity models are the favored choice to undertake microstructure based analysis and design well-performing materials with targeted properties. In this domain, the intrinsic hierarchical microstructural characteristics of martensite containing steels provide a focus of research not only for a length scale dependent plasticity model but also for a damage model capable of shedding light on damage and crack evolution in the microstructure.

Length scale dependent plasticity is indeed required when the size of the modeled constituents becomes close to the characteristic lengths of underlying plastic deformation mechanisms (Fleck and Hutchinson, 1997; Kocks and Mecking, 2003). Accounting for the storage of geometrically necessary dislocations (GND) arising from shear strain gradients can be used in order to incorporate such scale dependencies in crystal plasticity theories (Ashby, 1970; Acharya and Bassani, 2000). Models considering the full dislocation density tensor were developed for this purpose (Gurtin, 2002; Cordero et al., 2010; Kaiser and Menzel, 2019; Rys et al., 2020). These models were shown to be capable of predicting size-dependent hardening behaviors as well as to regularize shear band formation when strain softening occurs. In parallel, reduced gradient-enhanced crystal plasticity theories accounting for the gradients of a single scalar accumulated plastic slip variable were established (Wulfinghoff and Böhlke, 2012; Ling et al., 2018b; Scherer et al., 2019). This approach allows one to obtain less computationally demanding models, while still accounting for strain gradient contributions.

Two principally different approaches remain popular for introducing damage with crystal plasticity level analysis when considering cyclic loading, the so called fatigue indicator parameters (FIP) and evolution based damage models. FIPs usually utilize the stress–strain response of a crystal plasticity model and post-process prevailing state after certain number of loading cycles to extrapolate material failure and/or remaining (fatigue) lifetime. The computational cost in most cases is less for the FIP based models than for evolution based damage, at the expense of omitting grain-to-grain propagation of damage and its effect on the performance outcome. Nonetheless, considering the effectiveness of the FIP-models, it is possible to analyze causalities within the hierarchical martensitic microstructure (Schäfer et al., 2019; Li et al., 2016) or evaluate the effect of existing small and large defects (Pinomaa et al., 2019; Pineau and Forest, 2017).

Evolution based crystal plasticity damage models are rarer, much owing firstly to the complexity of fracture in general and secondly to the distinguishing constitutive relations between dislocation driven plasticity and damage or crack evolution. Effort has been placed on adapting classical continuum damage mechanics to crystal plasticity and degrading material's integrity during deformation with a plastic strain threshold value and evolution equation (Li et al., 2018; Zhao et al., 2019). In the same context, non-local crystal plasticity models are considered relevant to produce scaling effects and control of damage through a non-locality relation with dislocations, plastic strain, and defected area growth (Boeff et al., 2014, 2015; Abu Al-Rub et al., 2015; Kweon, 2016; Ling et al., 2018b; Scherer et al., 2019). In terms of brittle fracture, cleavage fracture based models introduce crystalline level informed damage with a stress based initiation criterion (Wu and Zikry, 2014), which can be extended with a softening evolution coupling damage and plasticity (Aslan et al., 2011a; Lindroos et al., 2019). In many occasions, the non-locality of the models approaches the scope of scale dependent hardening provided by geometrically necessary dislocations at sufficiently small grain sizes. Micromorphic models have been developed in order to address regularization of plasticity and damage (Brepols et al., 2017), while extensions to crystal plasticity were introduced to cope with the need of microstructure level predictions (Aslan et al., 2011a,b; Sabnis et al., 2016). Recent advancements also include the use of a coupled approach to describe damage evolution with phase field model and establish mechanical stress/strain state with a crystal plasticity model, including a capability to regularize damage (Tu and Ray, 2020). In order to account for size effects related to slip and address the regularization requirements of damage, there is a need to incorporate finite strain non-local plasticity behavior and damage regularization in the same model for brittle fracture in a computationally efficient way.

The micromorphic approach used in this work represents an extension of Eringen's original micromorphic theory (Eringen and Suhubi, 1964) to additional degrees of freedom other than Erigen's microdeformation tensor. Eringen, and Mindlin (Eringen and Suhubi, 1964; Mindlin, 1964) initially proposed to include the microdeformation of a triad of microstructure directors and its gradient into the continuum modeling. The micromorphic approach proposed by Forest (2009, 2016) introduces additional degrees of freedom and their gradient that can be related to micro-plastic and micro-damage variables. The advantage is that scalar degrees of freedom can be used instead of Eringen's full microdeformation tensor, so that computational efficiency can be improved. Since then, the method has been used by several authors, see for instance Poh et al. (2011), Brepols et al. (2017), in the case of isotropic plasticity and damage. This approach was also applied to single crystals considering the curl of a plastic microdeformation tensor (Cordero et al., 2010). However this model is very expensive since it involves 9 additional degrees of freedom at each node. That is why a reduced micromorphic model was then proposed by Ling et al. (2018a) making use of the gradient of a single scalar variable representing the cumulative plastic slip. This model was further developed by Scherer et al. (2019) for ductile damage applications. This reduced micromorphic model is explained in detail in the present work and extended to include new crystallographic damage mechanisms.

In line with this view, this work uses a finite strain reduced micromorphic crystal plasticity model to investigate non-local behavior of slip and damage in BCC metals. The novelty of the present approach is within the scale dependent regularization of plastic slip bands and crystalline level damage incorporated fully in the same model. Their interdependence is investigated in the context of lath martensitic steels. Special attention is placed on martensitic steels due to their inherent hierarchical strengthening

characteristics making them a suitable application with also practical engineering significance. First, single crystal cases are studied with and without the damage model in order to determine the influences of several material parameters on size effects and regularization of localized inelastic phenomena. In the second part, the size effects produced by the model in absence of damage are investigated for polycrystals to assess the arising scale dependent hardening. Then, the model behavior is further analyzed with a prior-austenite based polycrystalline microstructure quantifying damage effects. Throughout, a range of parameters is studied to infer model behavior and prepare for future efforts focusing on directly establishing material specific calibrations. Finally, a martensitic microstructure is introduced and the model's deformation and damage response are examined in this domain. Discussion focuses on the essence of the crystal plasticity-damage modeling scheme's suitability for polycrystals, especially on the application to modern martensitic steels. The choice of regularization method is finally reviewed in light of producing physically relevant length-scale dependent plasticity and damage response in a computationally efficient and tractable finite strain scheme.

2. Crystal plasticity model

2.1. Micromorphic approach

A finite strain framework is adopted in which the deformation gradient $\underline{\mathbf{F}}$ is multiplicatively decomposed into an elastic part $\underline{\mathbf{F}}^e$ and an inelastic part $\underline{\mathbf{F}}^i$.

$$\underline{\mathbf{F}} = \frac{\partial \underline{\mathbf{x}}}{\partial \underline{\mathbf{X}}} = \underline{\mathbf{F}}^e \cdot \underline{\mathbf{F}}^i \quad (1)$$

The velocity gradient $\underline{\mathbf{L}}$ comprises a purely elastic contribution and a contribution associated to inelastic deformation mechanisms.

$$\underline{\mathbf{L}} = \dot{\underline{\mathbf{F}}} \cdot \underline{\mathbf{F}}^{-1} = \dot{\underline{\mathbf{F}}}^e \cdot \underline{\mathbf{F}}^{e-1} + \underline{\mathbf{F}}^e \cdot \underline{\mathbf{L}}^i \cdot \underline{\mathbf{F}}^{e-1} \quad (2)$$

In the context of crystal plasticity the latter is classically decomposed into a sum of plastic slip rates $\dot{\gamma}^s$ over all slip systems (slip system number is denoted by superscript s). The direction of plastic slip rate is governed by the dislocations gliding directions $\underline{\mathbf{m}}^s$ and normal to slip planes $\underline{\mathbf{n}}^s$. Following Aslan et al. (2011a) additional inelastic rates are introduced in order to account for damage by crack opening rate $\dot{\delta}_c^k$ and crack shearing rates $\dot{\delta}_1^k$ and $\dot{\delta}_2^k$ (damage mechanism number is denoted by superscript k). The direction of damage rate is governed by the normal to cleavage planes $\underline{\mathbf{n}}_d^k$ and their in plane orthogonal directions $\underline{\mathbf{e}}_{-d1}^k$ and $\underline{\mathbf{e}}_{-d2}^k$.

$$\begin{aligned} \underline{\mathbf{L}}^i = \dot{\underline{\mathbf{F}}}^i \cdot \underline{\mathbf{F}}^{i-1} = & \sum_{s=1}^{N^s} \dot{\gamma}^s (\underline{\mathbf{m}}^s \otimes \underline{\mathbf{n}}^s) \\ & + \sum_{k=1}^{N_{damage}} \dot{\delta}_c^k (\underline{\mathbf{n}}_d^k \otimes \underline{\mathbf{n}}_d^k) + \dot{\delta}_1^k (\underline{\mathbf{e}}_{-d1}^k \otimes \underline{\mathbf{n}}_d^k) + \dot{\delta}_2^k (\underline{\mathbf{e}}_{-d2}^k \otimes \underline{\mathbf{n}}_d^k) \end{aligned} \quad (3)$$

In keeping with Wulfinghoff and Böhlke (2012) an equivalent plastic strain gradient enhancement of single crystal plasticity is adopted. The micromorphic approach (Forest, 2009) is followed in order to derive a finite strain crystal plasticity model which accounts for and regularizes plastic slip and/or damage. The variable γ_{cum} is introduced as the variable whose gradients will play a role in the constitutive behavior. Three different formulations are considered, for each of which the definition of γ_{cum} differs. The first considers plastic slip regularization only:

$$\gamma_{cum} = \int_0^t \sum_{s=1}^{N^s} |\dot{\gamma}^s| dt \quad (4)$$

The second accounts for both plastic slip and damage regularization:

$$\gamma_{cum} = \int_0^t \sum_{s=1}^{N^s} |\dot{\gamma}^s| dt + \int_0^t \sum_{k=1}^{N_{damage}} (|\dot{\delta}_c^k| + |\dot{\delta}_1^k| + |\dot{\delta}_2^k|) dt \quad (5)$$

The third involves damage regularization only:

$$\gamma_{cum} = \int_0^t \sum_{k=1}^{N_{damage}} (|\dot{\delta}_c^k| + |\dot{\delta}_1^k| + |\dot{\delta}_2^k|) dt \quad (6)$$

In all three cases, the non-local counterpart of γ_{cum} is denoted γ_χ and is treated as an additional degree of freedom. Therefore even when both slip and damage are regularized simultaneously, a single micromorphic variable is used. The Lagrangian gradient of γ_χ is denoted $\underline{\mathbf{K}}_\chi$.

$$\underline{\mathbf{K}}_\chi = \frac{\partial \gamma_\chi}{\partial \underline{\mathbf{X}}} \quad (7)$$

In conventional continuum mechanics the power of internal forces is $\underline{\mathcal{S}} : \dot{\underline{\mathbf{F}}}$, where $\underline{\mathcal{S}}$ denotes the first Piola–Kirchhoff stress related to the Cauchy stress by $\underline{\mathcal{S}} = \det(\underline{\mathbf{F}}) \underline{\boldsymbol{\sigma}} \underline{\mathbf{F}}^{-T}$. The standard principle of virtual power is extended to higher order contributions, namely

to contributions of γ_χ and $\underline{\mathbf{K}}_\chi$ which energetic counterparts are respectively the scalar stress S and vector stress $\underline{\mathbf{M}}$. In addition a generalized contact force M , conjugate to γ_χ is introduced. For any subdomain D_0 it is written as

$$\int_{D_0} (\underline{\mathbf{S}} : \underline{\dot{\mathbf{F}}} + S \dot{\gamma}_\chi + \underline{\mathbf{M}} \cdot \underline{\dot{\mathbf{K}}}_\chi) dV_0 = \int_{\partial D_0} (\underline{\mathbf{T}} \cdot \underline{\dot{\mathbf{u}}} + M \dot{\gamma}_\chi) dS_0 \quad \forall \underline{\dot{\mathbf{u}}}, \quad \forall \dot{\gamma}_\chi, \quad \forall D_0 \quad (8)$$

The application of Gauss' theorem leads to the balance equations

$$\text{Div } \underline{\mathbf{S}} = 0 \quad (9)$$

$$\text{Div } \underline{\mathbf{M}} - S = 0 \quad (10)$$

and associated boundary conditions, with surface normal $\underline{\mathbf{n}}_0$ in the reference configuration

$$\underline{\mathbf{T}} = \underline{\mathbf{S}} \cdot \underline{\mathbf{n}}_0 \quad (11)$$

$$M = \underline{\mathbf{M}} \cdot \underline{\mathbf{n}}_0 \quad (12)$$

The elastic Green–Lagrange strain $\underline{\mathbf{E}}_{GL}^e$ is introduced as follows

$$\underline{\mathbf{E}}_{GL}^e = \frac{1}{2} (\underline{\mathbf{F}}^{eT} \cdot \underline{\mathbf{F}}^e - \underline{\mathbf{1}}) \quad (13)$$

It is considered as a state variable involved in the elastic part of the free energy density. Other state variables are hardening variables involved in the hardening part of the free energy density. The hardening variables noted ρ^s , left to be defined, and the cumulated damage variable $d = \int_0^t \sum_{k=1}^{N_{damage}} \delta_c^k + \delta_1^k + \delta_2^k dt$ will be used as the hardening variables. Furthermore γ_{cum} , γ_χ and $\underline{\mathbf{K}}_\chi$ are the state variables involved in the nonlocal part of the free energy density. A quadratic form of the nonlocal free energy potential is chosen for simplicity. The higher order modulus A scales the material characteristic length. In addition a penalization term is introduced with the penalization modulus H_χ . In order to enforce quasi-equality between γ_{cum} and γ_χ a large value of the penalization modulus is usually used. The chosen specific free energy density is given by

$$\begin{aligned} \psi (\underline{\mathbf{E}}_{GL}^e, \rho^s, \gamma_{cum}, \gamma_\chi, \underline{\mathbf{K}}_\chi) = & \frac{1}{2\rho_\#} \underline{\mathbf{E}}_{GL}^e : \underline{\mathbf{C}} : \underline{\mathbf{E}}_{GL}^e + \psi_h(\rho^s, d) \\ & + \frac{A}{2\rho_0} \underline{\mathbf{K}}_\chi \cdot \underline{\mathbf{K}}_\chi + \frac{H_\chi}{2\rho_0} (\gamma_{cum} - \gamma_\chi)^2 \end{aligned} \quad (14)$$

$\rho_\#$ and ρ_0 denote the volumetric mass density in the intermediate and initial configurations respectively. It must be noted that the non-local contribution to the free energy, namely the two last terms in Eq. (14), depend on the choice of the expression of γ_{cum} that is made. If Eq. (4) is chosen, only plastic slip gradients play a role in the free energy density, while if Eq. (6) is used, only damage gradients play a role in the free energy density. When Eq. (5) is considered, it is gradients of the cumulated damage and slip variable which come into play in the free energy density. The Clausius–Duhem inequality obtained from 1st and 2nd principles of thermodynamics enforces

$$\frac{\underline{\mathbf{S}}}{\rho_0} : \underline{\dot{\mathbf{F}}} + \frac{S}{\rho_0} \dot{\gamma}_\chi + \frac{\underline{\mathbf{M}}}{\rho_0} \cdot \underline{\dot{\mathbf{K}}}_\chi - \dot{\psi} \geq 0 \quad (15)$$

The first term on left-hand side of Eq. (15) can be reformulated in terms of the following stress measures

$$\underline{\mathbf{\Pi}}^e = \det(\underline{\mathbf{F}}^e) \underline{\mathbf{F}}^{e-1} \cdot \underline{\sigma} \cdot \underline{\mathbf{F}}^{e-T} = \det(\underline{\mathbf{F}}^e) \underline{\mathbf{F}}^{e-1} \cdot \underline{\mathbf{S}} \cdot \underline{\mathbf{F}}^{iT} \quad (16)$$

$$\underline{\mathbf{\Pi}}^M = \underline{\mathbf{F}}^{eT} \cdot \underline{\mathbf{F}}^e \cdot \underline{\mathbf{\Pi}}^e \quad (17)$$

where $\underline{\mathbf{\Pi}}^M$ is Mandel's stress tensor. Eq. (15) becomes

$$\frac{\underline{\mathbf{\Pi}}^e}{\rho_\#} : \underline{\dot{\mathbf{E}}}_{GL}^e + \frac{\underline{\mathbf{\Pi}}^M}{\rho_\#} : (\underline{\dot{\mathbf{F}}}^i \cdot \underline{\mathbf{F}}^{i-1}) + \frac{S}{\rho_0} \dot{\gamma}_\chi + \frac{\underline{\mathbf{M}}}{\rho_0} \cdot \underline{\dot{\mathbf{K}}}_\chi - \dot{\psi} \geq 0 \quad (18)$$

Following the Coleman–Noll procedure the state laws are postulated

$$\underline{\mathbf{\Pi}}^e = \rho_\# \frac{\partial \psi}{\partial \underline{\mathbf{E}}_{GL}^e} = \underline{\mathbf{C}} : \underline{\mathbf{E}}_{GL}^e \quad (19)$$

$$S = \rho_0 \frac{\partial \psi}{\partial \gamma_\chi} = -H_\chi (\gamma_{cum} - \gamma_\chi) \quad (20)$$

$$\underline{\mathbf{M}} = \rho_0 \frac{\partial \psi}{\partial \underline{\mathbf{K}}_\chi} = A \underline{\mathbf{K}}_\chi \quad (21)$$

When both plastic slip and damage are accounted for in the definition of γ_{cum} , the residual mechanical dissipation can hence be written

$$\begin{aligned}
 d = & \sum_{s=1}^{N^s} \left(|\tau^s| + \frac{\rho_{\#}^s}{\rho_0} S \right) |\dot{\gamma}^s| - \rho_{\#}^s \frac{\partial \psi_h}{\partial \rho^s} \dot{\rho}^s \\
 & + \sum_{k=1}^{N_{damage}} \left(|\sigma_{dc}| + \frac{\rho_{\#}^k}{\rho_0} S - \rho_{\#}^k \frac{\partial \psi_h}{\partial d} \right) |\dot{\delta}_c^k| \\
 & + \sum_{k=1}^{N_{damage}} \left(|\tau_{d1}^k| + \frac{\rho_{\#}^k}{\rho_0} S - \rho_{\#}^k \frac{\partial \psi_h}{\partial d} \right) |\dot{\delta}_1^k| \\
 & + \sum_{k=1}^{N_{damage}} \left(|\tau_{d2}^k| + \frac{\rho_{\#}^k}{\rho_0} S - \rho_{\#}^k \frac{\partial \psi_h}{\partial d} \right) |\dot{\delta}_2^k|
 \end{aligned} \tag{22}$$

where τ^s is the resolved shear stress on slip system s , σ_{dc} is the opening stress for a cleavage plane, τ_{d1}^k and τ_{d2}^k are shear stresses on the cleavage planes. The damage model is further reviewed in the following sections.

However, if only plastic slips are considered to define γ_{cum} the term $(\rho_{\#}^s/\rho_0)S$ vanishes from the three last terms in Eq. (22). On the contrary, if only damage is used to define γ_{cum} the term $(\rho_{\#}^k/\rho_0)S$ vanishes from the first sum in Eq. (22). Positivity of the dissipation in all these three cases will be ensured by the choice of adequate yield and damage criteria presented in following section.

2.2. Single crystal model

The single crystal model follows the general principles of our previous work focusing on fatigue damage formulation of martensitic steels using conventional crystal plasticity framework (Lindroos et al., 2019). A gradient plasticity extension and applied modifications on the damage model are presented in the following. Inelastic strain rate consist in the sum of plastic slip of dislocations and a strain-like contribution due to damage. A strain-like formulation of damage presents the benefits of allowing the tracking of opening and closure of cracks and of being straightforwardly embedded in the present micromorphic crystal plasticity model. The form presented in Eq. (3) may be expressed as an additive decomposition:

$$\underline{\mathbf{L}}^i = \underline{\mathbf{L}}^p + \underline{\mathbf{L}}^d \tag{23}$$

The contribution of dislocation slip responsible of plastic deformation is given by:

$$\underline{\mathbf{L}}^p = \sum_{s=1}^{N^s} \dot{\gamma}^s (\underline{\mathbf{m}}^s \otimes \underline{\mathbf{n}}^s) \tag{24}$$

The slip rate is provided by a rate dependent form

$$\dot{\gamma}^s = \dot{v}^s \text{sign}(\tau^s) = \left\langle \frac{|\tau^s| - (r^s + \tau_0 - S)}{K} \right\rangle^n \text{sign}(\tau^s) \tag{25}$$

where $\langle \cdot \rangle$ are Macaulay brackets, material parameters K and n characterize the viscosity, $v^s = \int_0^t |\dot{\gamma}^s| dt$, and $\tau^s = \underline{\mathbf{n}}_s \cdot \underline{\mathbf{II}}^M \cdot \underline{\mathbf{e}}_{-s}$, are the current cumulative slip and resolved shear stress in a system s , respectively. Slip plane normal is denoted with $\underline{\mathbf{n}}_s$ and slip direction by $\underline{\mathbf{e}}_{-s}$. τ_0 is the initial shear resistance of slip system families $\{110\} \langle 111 \rangle$ and $\{112\} \langle 111 \rangle$. For simplicity, the initial shear resistance is assumed the same for both slip families. r^s is the isotropic hardening term derived from ψ_h , and S is the generalized stress. S only appears in Eq. (25) if plastic slips are accounted for to define γ_{cum} and is thus absent if damage regularization only (i.e. Eq. (6)) is considered. Following the nonlinear form suggested by Aslan et al. (2011a), the hardening potential $\psi_h(\rho^s, d)$ unspecified in Eq. (14) is supposed to take the following expression

$$\begin{aligned}
 \psi_h(\rho^s, d) &= \frac{1}{2\rho_0} Q \sum_{i=1}^{N^s} (\rho^i)^2 + \frac{\sigma_c^0 d}{\rho_0} \exp\left(-\beta \sum_{s=1}^{N^s} v^s\right) + \frac{1}{2\rho_0} H d^2 \\
 &= \frac{1}{2\rho_0} Q \sum_{i=1}^{N^s} \left(\sum_{j=1}^{N^s} H_{ij} (1 - \exp(-bv^j)) - \frac{\sigma_c^0 \beta d}{Q} \exp\left(-\beta \sum_{j=1}^{N^s} v^j\right) \right)^2 \\
 &\quad + \frac{\sigma_c^0 d}{\rho_0} \exp\left(-\beta \sum_{s=1}^{N^s} v^s\right) + \frac{1}{2\rho_0} H d^2
 \end{aligned} \tag{26}$$

where the chosen expression of the hardening variables ρ^i is defined in Eq. (27). H_{ij} is the slip-slip interaction matrix (24×24) for which only 8 independent coefficients h_1, \dots, h_8 are considered (Hoc and Forest, 2001) (see Table 1). σ_c^0 is the initial cleavage resistance, and β is the coupling factor relating slip and damage mechanisms. Isotropic hardening arises from dislocation interactions and damage is assumed to soften the slip resistance after damage initiation. The hardening terms take the following expression

$$r^i = \rho_0 \frac{\partial \psi_h}{\partial \rho^i} = Q \sum_{j=1}^{N^s} H_{ij} (1 - \exp(-bv^j)) - \sigma_c^0 \beta d \exp\left(-\beta \sum_{j=1}^{N^s} v^j\right) \tag{28}$$

Exponential form results from the choice of free energy potential that couples slip and damage activities. Accumulation of slip is assumed to decrease the cleavage resistance, as it becomes clear in the presentation of the damage formulation hereafter. The damage contribution to inelastic strain is a sum of three damage mechanism related contributions.

$$\underline{\underline{L}}^d = \sum_{k=1}^{N_{damage}} \delta_c^k (\underline{\underline{n}}_d^k \otimes \underline{\underline{n}}_d^k) + \delta_1^k (\underline{\underline{\ell}}_{d1}^k \otimes \underline{\underline{n}}_d^k) + \delta_2^k (\underline{\underline{\ell}}_{d2}^k \otimes \underline{\underline{n}}_d^k) \quad (29)$$

where δ_c^k , δ_1^k , δ_2^k are the strain rates for mode I like crack opening, mode II and mode III shear crack growth, respectively. The number of damage planes is noted N_{damage} . In the following, $\{100\}$ crystallographic planes will be considered as the cleavage planes existing in a BCC crystal structure. Cleavage damage is activated by the opening δ_c of cleavage planes with the normal vector $\underline{\underline{n}}_d^k$. Shear damage accommodate in-plane deformation in orthogonal directions $\underline{\underline{\ell}}_{d1}^k$ and $\underline{\underline{\ell}}_{d2}^k$. The evolution of the opening rate is given by:

$$\delta_c^k = \left\langle \frac{|\sigma_{dc}| - (Y_c^k - S)}{K_d} \right\rangle^{n_d} \text{sign}(\sigma_{dc}) \quad \text{with} \quad \sigma_{dc} = \underline{\underline{n}}_d^k \cdot \underline{\underline{\Pi}}^M \cdot \underline{\underline{n}}_d^k \quad (30)$$

Crack opening damage strain δ_c^k becomes active when the cleavage opening resistance Y_c^k is exceeded by the normal stress σ_{dc} acting on the cleavage planes. The strain like treatment of the opening damage allows to track crack closure. In the spirit of smeared crack behavior the constraint that $\delta_c^k \geq 0$ is imposed, in order to prevent crack opening when the opening stress is negative. The rates of damage shear mechanisms use the same rate dependent formulation:

$$\delta_i^k = \left\langle \frac{|\tau_{di}| - (Y_i^k - S)}{K_d} \right\rangle^{n_d} \text{sign}(\tau_{di}) \quad \text{with} \quad \tau_{di} = \underline{\underline{n}}_d^k \cdot \underline{\underline{\Pi}}^M \cdot \underline{\underline{\ell}}_{di}^k \quad (31)$$

where shear stress τ_{di} activates the damage shear mechanisms after shear resistance Y_i^k is met. Viscous parameters K_d and n_d are taken to be same for crack opening and shearing mechanisms. S only appears in Eq. (30) and (31) if damage mechanisms are accounted for to define γ_{cum} and is thus absent if slip regularization only (i.e. Eq. (4)) is considered.

Cleavage is expected to occur in the region with large plastic activity. Shear localization therefore reduces cleavage resistance and promotes damage initiation at these sites. After damage initiation, the cleavage resistance also decreases with the linear softening modulus H . Cleavage resistance is set to be always positive for numerical reasons with a constraint that $Y_c^k \geq \sigma_{ult}$, where residual strength σ_{ult} is chosen small, for example $\sigma_{ult} = \sigma_c^0/200$.

$$Y_c^k = Y_i^k = \rho_0 \frac{\partial \psi_h}{\partial d} = \sigma_c^0 \exp\left(-\beta \sum_{s=1}^{N^s} v^s\right) + Hd \quad (32)$$

Regularization established with the generalized stress can then be chosen to adapt on slip alone, regularizing slip band formation and generating plasticity size effects. The effect on damage is indirect through the control of plasticity affected regions. Damage regularization may be achieved directly by introducing a contribution of the generalized stress term into the cleavage resistance. This is achieved by accounting for the definition of γ_{cum} at Eq. (6). This formulation also regularizes plastic slip indirectly by affecting the damage related softening of the slip resistance. If the cumulative inelastic variable is chosen to account for both slip and damage as in Eq. (5), the regularization is hybrid, affecting and creating direct coupling between both inelastic mechanisms. The following section reviews some of the characteristics of these alternatives.

3. Results

The model was implemented in the finite element software Z-set (Besson and Foerch, 1998; Z-set package, 2013). The constitutive behavior is discretized following a forward-Euler scheme and integration is achieved with a Runge–Kutta algorithm. In order to validate the finite element implementation in absence of damage, numerical predictions were compared to analytical solutions derived on a two-phase laminate in the spirit of Forest (2008). Details on this benchmark example are presented in Appendix A. Influence of the key material parameters are analyzed below.

3.1. Single crystal case with damage

A single crystal perforated plate of width L_0 , and cylindrical void radius R_0 , is loaded in tension as depicted in Fig. 1. The initial void volume fraction, defined as $\pi R_0^2/L_0^2$, is equal to 1%. The orientation of the BCC single crystal is defined with respect to the orthonormal basis ($\underline{\underline{X}}_1, \underline{\underline{X}}_2, \underline{\underline{X}}_3$) attached to the specimen. Three dimensional brick elements with reduced integration at 8 Gauss points are used. The displacement degrees of freedom are interpolated with quadratic shape functions and the microslip degrees of freedom γ_χ are interpolated with linear shape functions. After (Hoc and Forest, 2001), the number of independent coefficients is reduced to eight in the 24×24 interaction matrix by classifying the slips systems belonging to the same slip family into collinear and non-collinear systems. These coefficients are noted h_i with $i = 1..8$ as presented in Table 1. Numerical values of material parameters are listed in Table 2. Convergence with respect to mesh size was checked as presented in Appendix B and showed that predictions are already converged with a mesh composed of 400 elements and 9880 degrees of freedom. Unless otherwise stated crystal axes [100], [010] and [001] are initially respectively aligned with the basis vectors $\underline{\underline{X}}_1$, $\underline{\underline{X}}_2$ and $\underline{\underline{X}}_3$.

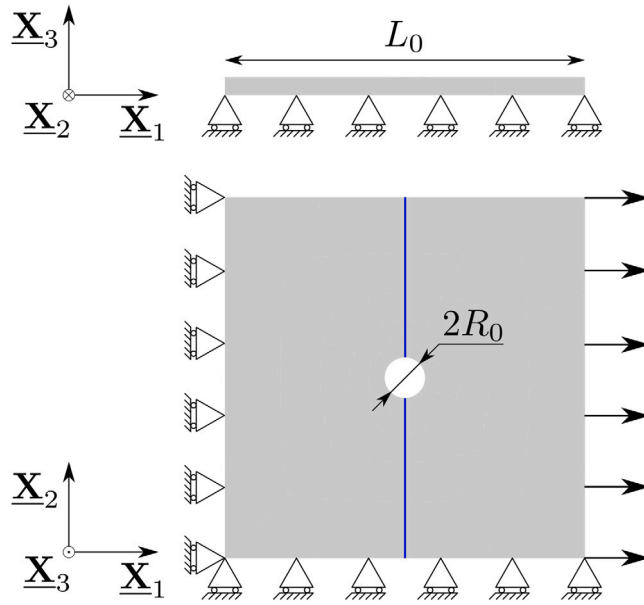


Fig. 1. Single crystal perforated plate geometry and applied boundary conditions.

Table 1
Coefficients for the interaction matrix in BCC crystals (Hoc and Forest, 2001).

Plane	{110} ∩ {110}	{110} ∩ {112}	{112} ∩ {112}
Same	h_8	–	h_1
Collinear	h_2	h_3	h_6
Non-collinear	h_4	h_5	h_7

Table 2
Numerical values of material parameters for single crystal model used in single and polycrystal simulations. h_i are interaction matrix coefficients.

Parameter	Value	Unit
Elastic constants		
C_{11}	197 000	[MPa]
C_{12}	134 000	[MPa]
C_{44}	105 000	[MPa]
Slip parameters		
τ_0^*	163	[MPa]
K	163	[MPa s ^{1/n}]
n	30	[MPa]
b	19	–
Q	30	–
h_1	1.3	–
h_2	1.0	–
h_3	1.05	–
h_4	1.15	–
h_5	1.1025	–
h_6	1.3	–
h_7	1.495	–
h_8	1.0	–
Damage parameters		
σ_c^0	2100	[MPa]
K_d	50	[MPa s ^{1/n_d}]
n_d	3	–
H	–1750	[MPa]
β	5	–
Gradient parameters		
H_x	10 ³ –10 ⁷	[MPa]
A	0; 1; 10; 100; 1000	[N]

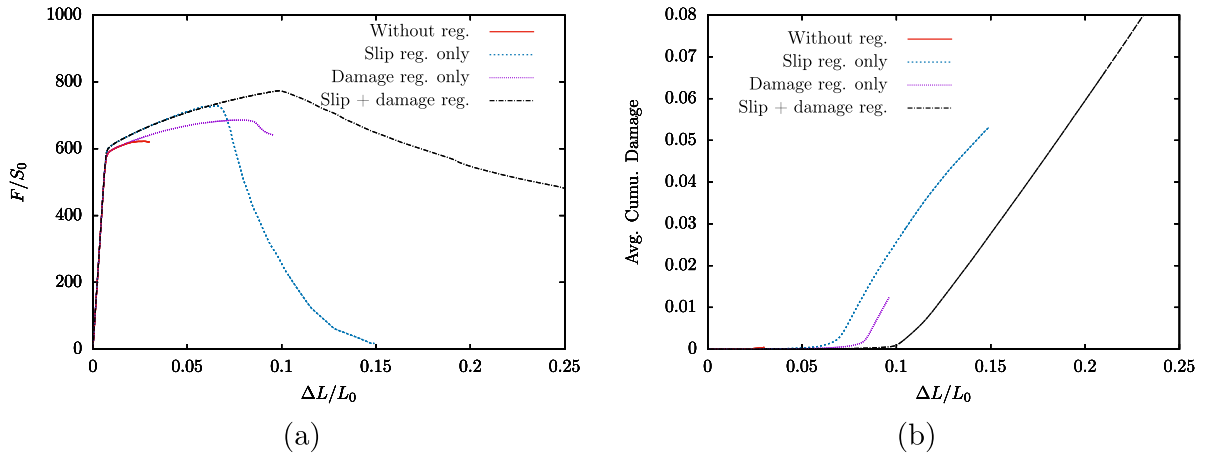


Fig. 2. Influence of the chosen variable for gradient regularization on (a) the stress–strain behavior and (b) average cumulated damage evolution for a $[100] - [010] - [001]$ crystal orientation. H_x is set to 10^4 MPa.

Importance of the variable on which regularization operates is first assessed. Three different definitions of the scalar variable γ_{cum} bearing gradient effects were given in Eq. (4), (5) and (6). Each formulation is used in the perforated plate specimen example with the same initial crystal orientation and material parameters. Simulations were run with the mesh composed of 400 elements. The same test is also performed without any regularization. Fig. 2 shows the macroscopic stress–strain and average cumulated damage responses. The choice of the regularized variable definition appears critical since very distinct behaviors are observed for each definition. When only plastic slip is regularized (Eq. (4)) acceleration of damage sets on the earliest and consequently the macroscopic stress drops the earliest. This is due to the fact that damage is only indirectly smoothed out by the strain gradient hardening induced by plastic slip localization. When only damage is regularized (Eq. (5)) steepening of the average cumulated damage evolution occurs at slightly larger macroscopic strains. Therefore macroscopic softening is also slightly postponed as compared to slip-only regularization. In this case, damage localization is directly penalized and plastic slip localization is indirectly smoothed out by damage localization induced hardening. When both slip and damage variables are regularized (Eq. (6)), average cumulated damage acceleration is again postponed as compared to the case when only one of the two variables is considered for regularization. Nevertheless the slope of cumulated damage increase is almost identical for the three regularization options. On the contrary the softening regime observed with the combined slip and damage regularization is much less abrupt. Influence of the choice of the regularization variable will be further investigated and discussed on polycrystals simulations presented in Sections 3.3 and 3.4.

The influence of higher order moduli H_x and A are investigated. The penalty modulus H_x serves to penalize the difference between γ_{cum} and γ_x . Therefore the larger H_x is, the lower this difference is. Usually a large value is used so that the micromorphic formulation approaches results corresponding to conventional strain gradient plasticity which is the limit case when H_x goes to infinity. Five different values of H_x , ranging from 10^3 to 10^7 MPa, are considered. Fig. 3(a) displays how H_x plays on the macroscopic hardening behavior. It can be observed that the macroscopic apparent yield stress is not affected by the value of H_x . However increasing H_x results in a larger apparent hardening modulus. Although convergence in terms of H_x value was not attained, it is expected that when increasing H_x a saturation of the increase of the hardening slope would eventually be reached. A corollary effect can be noted on the average cumulated damage curves plotted in Fig. 3(b). For the lowest H_x value of 10^3 MPa, damage acceleration sets on the earliest. However for larger H_x values it can be observed that the higher H_x is, the earlier average damage starts to accelerate and simultaneously macroscopic stress starts to drop. Once damage accelerated, the slopes of damage evolution are parallel to one another for H_x values ranging from 10^4 to 10^7 MPa. Yet, increasing the value of H_x raises significantly the computation time. This is due to the fact that increasing H_x forces to reduce the time steps when integrating the plastic slip evolution equations in which the higher order stress $S = H_x(\gamma_x - \gamma_{cum})$ is involved. The choice of a suitable H_x value is hence a competition between desired scaling behavior and affordable computational effort.

The higher order modulus A (unit MPa mm²) contains the characteristic length of the medium. Conventional plasticity, not accounting for strain gradient effects, corresponds to a medium with a vanishing characteristic length with $A = 0$ MPa mm². Increasing A amounts to increase this intrinsic length. In order to characterize the effect of A on regularization of slip and damage we consider three different crystal orientations, respectively having the triplet of crystal directions $([100], [010], [001])$, $([110], [\bar{1}10], [001])$ and $([111], [\bar{2}11], [0\bar{1}1])$ aligned with the orthonormal basis $(\underline{X}_1, \underline{X}_2, \underline{X}_3)$. For each orientation several values of A are used ranging between 0 MPa mm² and 1000 MPa mm². Fig. 4 displays macroscopic stress–strain and average cumulated damage curves obtained for each crystal orientation and A values. The main features to be noted is that A plays an important role simultaneously on the hardening behavior, on strain at damage onset and softening behavior. When A is increased a stronger apparent strain hardening is observed, damage onset is postponed and softening rate is reduced. It can interestingly be remarked that intensity of the effect of A varies with the initial crystal orientation. A significant influence of A is visible on hardening and strain at damage onset for crystal

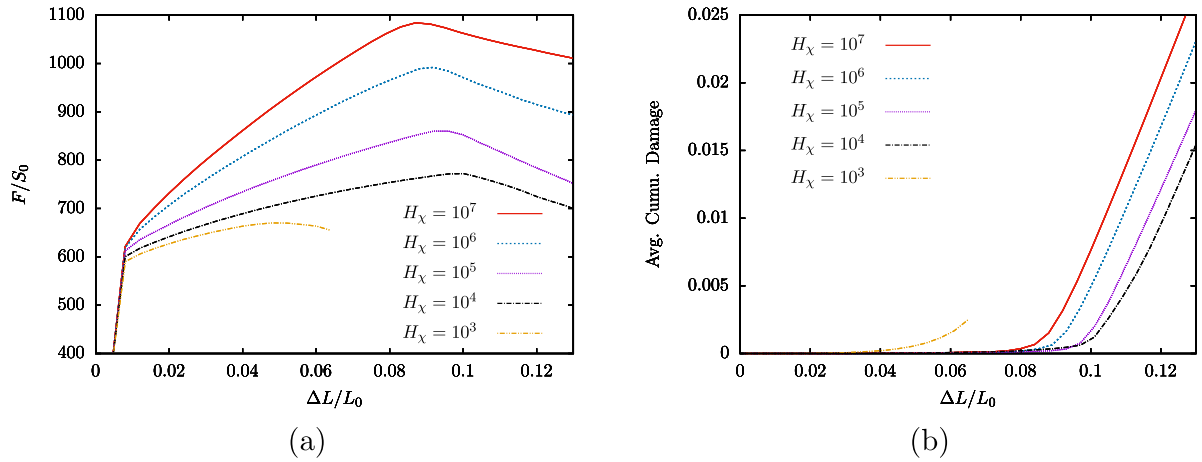


Fig. 3. Influence of penalty modulus H_χ on (a) the stress–strain behavior and (b) average cumulated damage evolution for a [100] – [010] – [001] crystal orientation.

orientations ([100], [010], [001]) and ([111], $[\bar{2}11]$, $[0\bar{1}1]$). However for crystal orientation ([110], $[\bar{1}10]$, [001]) almost no influence of A is observed on the behavior prior to damage onset. For the three crystal orientations, a larger value of A results in a slower acceleration of damage. In addition, when comparing results with $A = 100 \text{ MPa mm}^2$ and $A = 1000 \text{ MPa mm}^2$ a saturation of the size effect induced by A seems to have been reached in this example since stress–strain and average cumulated damage curves are almost superimposed.

The effect of A on damage fields is of paramount importance. The aim of this strain gradient model to regularize simultaneously slip and damage quantities can be assessed by comparing results when A vanishes (conventional plasticity) and when it takes values different from zero. Fig. 5 shows the contours of damage fields for each crystal orientation and for several values of A . When $A=0 \text{ MPa mm}^2$ damage is localized in the vicinity of the hole and forms a very thin band oriented perpendicularly to the loading direction. The width of this localization band is mesh-size dependent. However when strain or damage gradients are accounted for (*i.e.* $A \neq 0$) the localization band spreads over a larger distance along the tensile direction and perpendicularly to the tensile direction. In this case results are no longer mesh-size dependent (owing to the fact that convergence was reached as shown in Appendix B). It can be observed that orientation of the regularized damage localization band is not only affected by the main loading direction but also by the initial crystal orientation. The damage localization band appears slanted for the ([100], [010], [001]) orientation, while it remains perpendicular to the loading direction for the ([111], $[\bar{2}11]$, $[0\bar{1}1]$) orientation. The largest A value causes damage to spread over almost the whole geometry. However, and although saturation of macroscopic size effects seems to have been reached, some gradients of damage still persist.

A description of the role of parameter β and H involved in the evolution of cleavage resistance defined at Eq. (32) is given in Appendix C.

3.2. Scaling effects in polycrystals

To demonstrate the grain-to-grain strengthening behavior of the model, a polycrystalline microstructure is introduced. The polycrystal includes 50 non-equal sized grains all having different orientation. This setting reduces martensitic microstructure greatly to only include prior austenite grains for the sake of simplicity. Kinematic uniform boundary conditions are imposed for a uniaxial tensile simulation, as is presented in Fig. 6h. All meshes are 3D with one element in the thickness direction. At grain boundaries, continuity of displacement and microslip degrees of freedom are considered. In addition, continuity of usual tractions ($\sigma \cdot \underline{n}$, with \underline{n} the grain boundary normal) and generalized tractions ($\underline{M} \cdot \underline{n}$) are used. Other possibilities would be to consider so-called microhard interface conditions ($\gamma_\chi = 0$) or microfree interface conditions ($\underline{M} \cdot \underline{n} = 0$) as proposed by Gurtin (2004).

Fig. 6 demonstrates the scaling capability of the model for a polycrystalline microstructure with two values of H_χ in an uniaxial tensile test. Although the model does not predict a scaling of initial critical resolved shear stress, the curves show an apparent increase in yield strength. That increase is introduced by microplasticity and related strain gradient induced hardening. It is observed that the reduced gradient model produces a *tanh*-shaped scaling law with a capability to saturate at diminishing small grain sizes that contrast the unbounded increase in flow stress of conventional strain gradient plasticity (see also the analytical scaling law obtained on the two-phase laminate in Appendix A). The stress–strain curves homogenized over the whole polycrystal show varying hardening responses depending on the chosen micromorphic gradient parameters. As expected, a larger H_χ value generates greater hardening response. The modulus A scales the material intrinsic length and thereby increasing A , at a given microstructure size, results in a harder response. Fig. 6g contains early plasticity comparison between experimental and simulated tensile stress–strain curve. The model parameters were set based on previous non-gradient crystal plasticity study (Lindroos et al., 2019), but with a

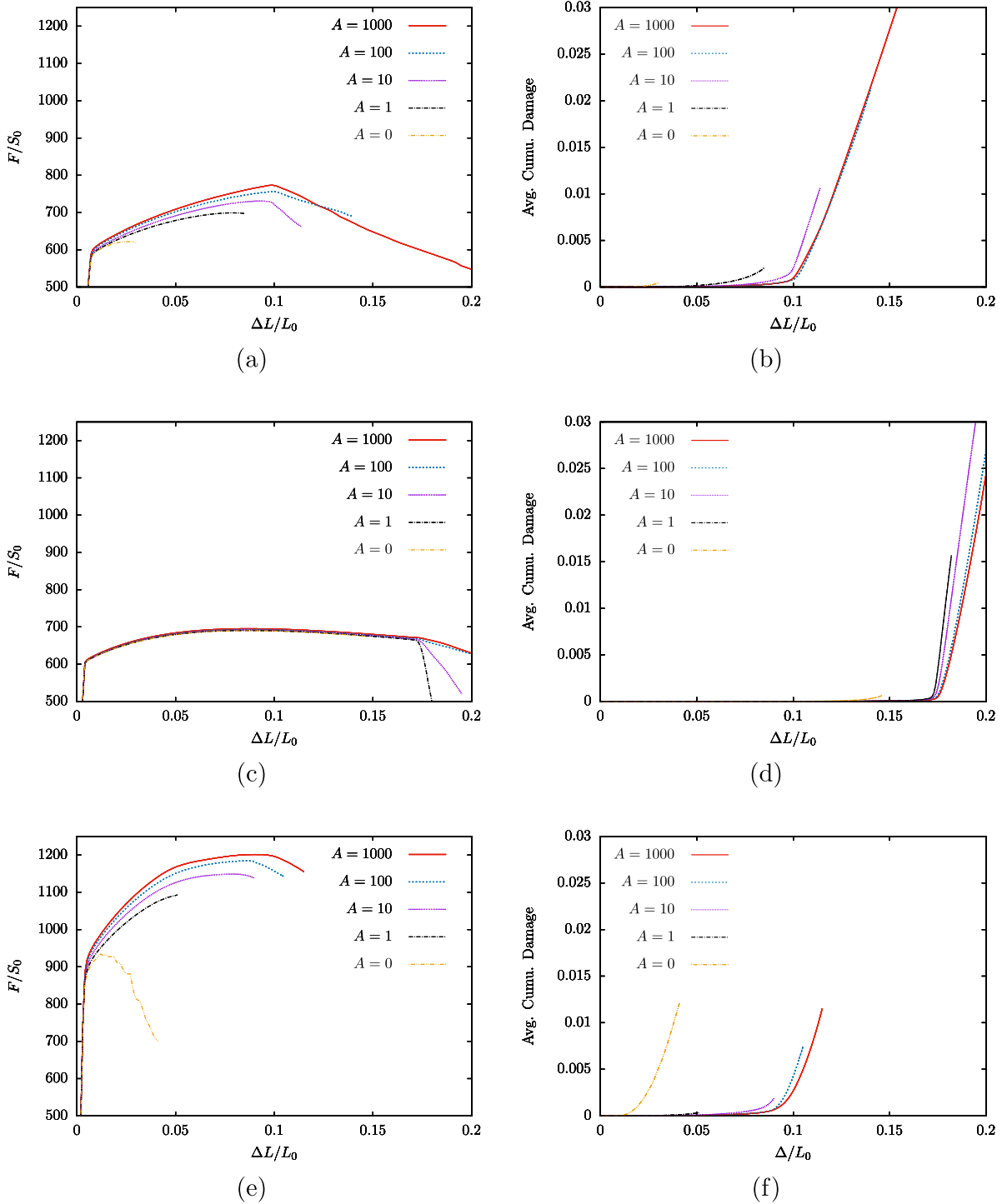


Fig. 4. Influence of parameter A on macroscopic stress–strain and average cumulated damage curves for crystal directions $([100],[010],[001])$ in (a–b), $([110],[\bar{1}\bar{1}0],[001])$ in (c–d) and $([111],[\bar{2}11],[0\bar{1}\bar{1}])$ in (e–f). H_χ is set to 10^4 MPa.

low amount of length-scale hardening i.e., $A = 0.1$ MPa mm² and $H_\chi = 10^4$ MPa, to distinguish the length-scale hardening effect with different parametrization.

Fig. 7 visualizes conventional crystal plasticity response and several gradient plasticity cases at 5% of macroscopic strain. At grain boundaries, interface conditions are chosen such as to have continuity of displacements and microslip, as well as usual and

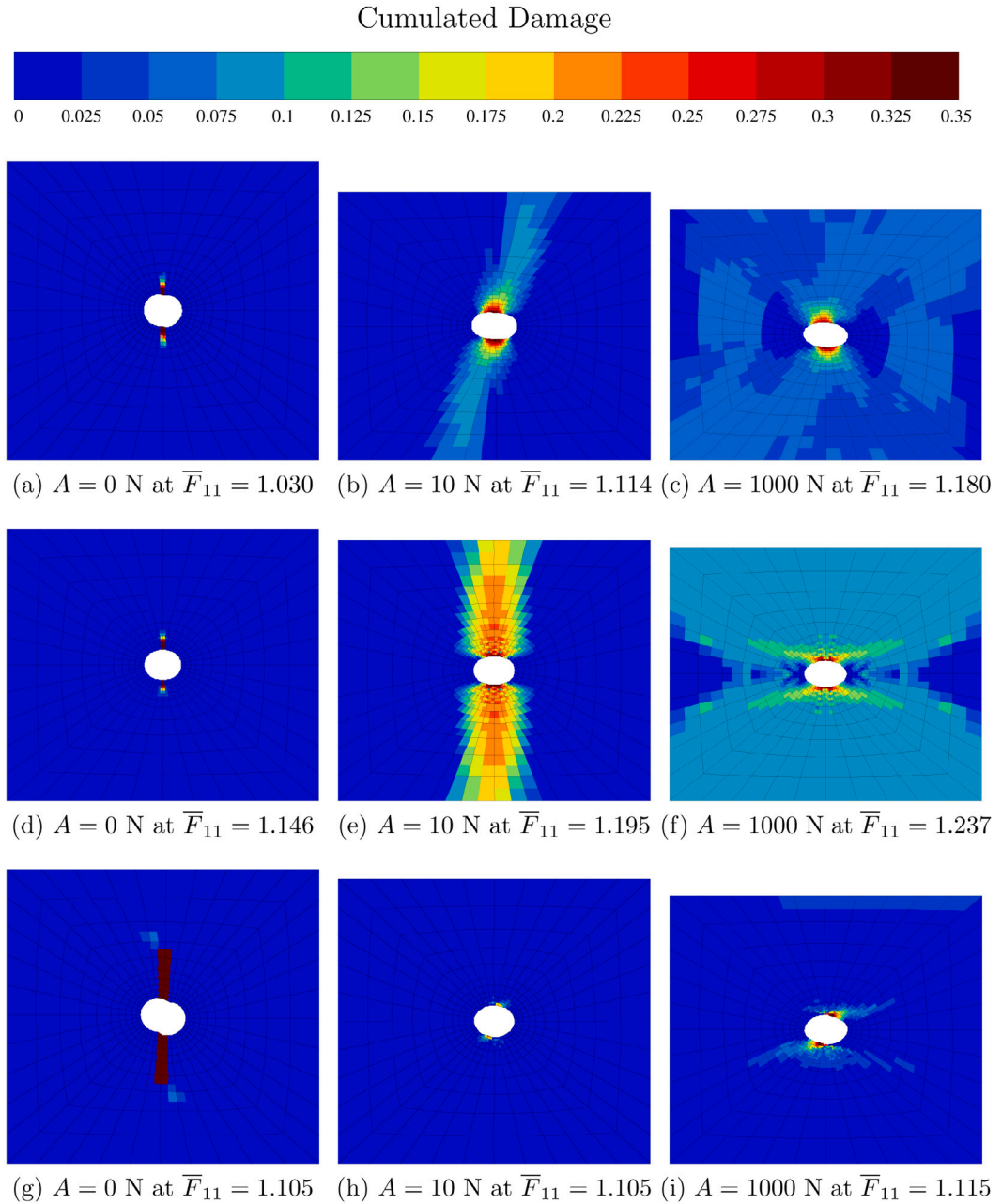


Fig. 5. Influence of parameter A on damage variable fields for crystal directions $([100],[010],[001])$ in (a–c), $([110],[\bar{1}10],[001])$ in (d–f) and $([111],[\bar{2}11],[0\bar{1}1])$ in (g–i). $A = 0$ N in (a, d, g), $A = 10$ N in (b, e, h) and $A = 1000$ N in (c, f, i). H_y is set to 10^4 MPa.

generalized tractions. As expected, regularization is established with variations in generalized stress in the region with a high plastic mismatch, such as the vicinity of grain boundaries and at zones prone to slip localization. As a limiting low-end case, the non-regularized response with conventional crystal plasticity shows more freedom in developing higher magnitude of slip in plasticity dominated regions and the grain boundary region hardening is significantly smaller than for the gradient cases. Cumulative slip in the gradient cases becomes more diffuse because of the penalized development of strain gradients in the analyzed microstructure. The smallest of the two investigated aggregate sizes, 1.0 mm and 0.1 mm, represents a case, whose deformation response is strongly influenced by the scaling effects, as seen in Fig. 7b. The generalized stress term gains more importance and the equivalent stress appears more spreading. This spreading is of similar type to the one observed with the norm of dislocation density tensor (Forest, 2008), in which this norm value is higher close to grain boundaries and begins to spread towards interiors of the grains with

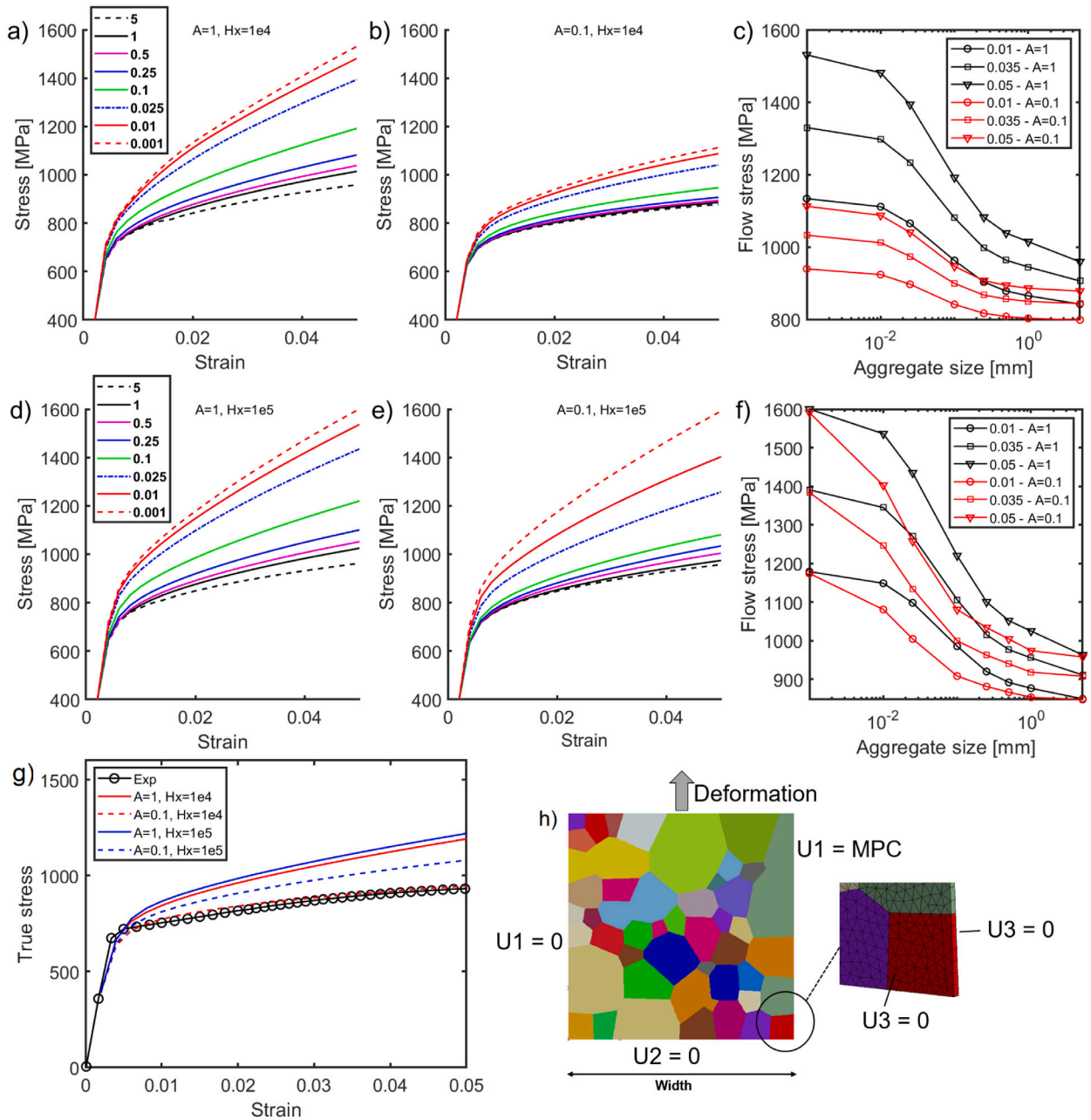


Fig. 6. Stress–strain evolution and scaling effects of different polycrystal aggregate sizes. Scaling laws in (c) and (f) are plotted for three different values of macroscopic strain, namely 0.01, 0.035 and 0.05. Hardening response of the model is adjusted with the experimental curve using $H_\gamma = 10^4$ MPa and $A = 0.1$ MPa mm² as baseline with corresponding prior austenite grain size to QT-steel (Lindroos et al., 2019). Polycrystalline aggregate in (h) is scaled in the simulations. Numbers in legends of figure (a) and (d) refer to aggregate width in [mm].

decreasing grain size. The characteristic length-scale, estimated with $\ell_c = \sqrt{A/H_\gamma}$, plays a crucial role in the saturation of size effects. When the grain size is getting close to this value, gradient-induced hardening begins to saturate.

Plastic deformation responses of conventional crystal plasticity and strain gradient plasticity are very distinct in the plots tracked along a certain path in the microstructure, which is shown in Fig. 8. Denotation “sc.” throughout the work refers to width of the polycrystalline RVE, e.g., sc. 1.0 refers to the microstructure of width 1.0 mm. Plastic slip concentrations are observed for both cases over the chosen region in Fig. 8c, yet the gradient plasticity case displays smoother distribution of plastic slip. Fig. 8d shows that stress concentrations develop near the grain boundary as a result of the plastic incompatibility between two grains. The phenomenological basis of the constitutive equations in the present work does not explicitly use dislocation densities. However, the

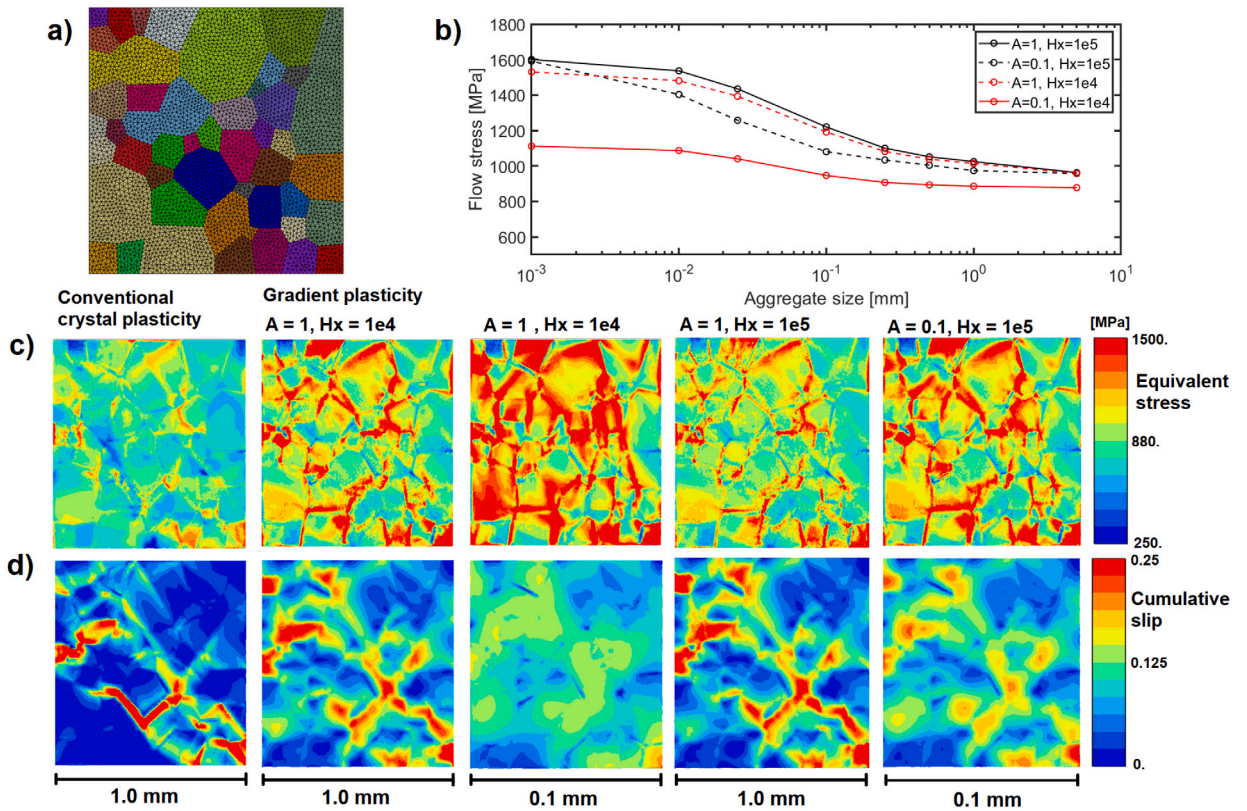


Fig. 7. (a) Computational polycrystal mesh, (b) scaling effects on flow stress at 5% of axial strain generated by gradient parametrization, (c) Von Mises stress contours, and (d) cumulative slip contours for two polycrystal size scales and with different gradient plasticity parametrization.

results indicate that the gradient model is capable of bringing the significant extra-hardening generally related to the evolution of geometrically necessary dislocations at grain boundaries within the reach of the current model in a phenomenological sense. It is worth noting, however, that the interpretation of the single gradient variable is less intuitive than gradient variables used in other models. For instance, there is not a direct straightforward link such as the relation which exist between the curl of the plasticity tensor and the dislocation density tensor (Rys et al., 2020; Cordero et al., 2013).

3.3. Damage behavior of polycrystals

The following addresses damage behavior provided by the model in a polycrystalline structure as an extension of the single crystal analyses. Fig. 9 shows stress–strain responses and damage evolution of non-regularized and regularized cases for two values of H^x . Non-regularized slip with conventional crystal plasticity has a tendency to activate damage earlier because of the faster developing of localized slip zones. By reducing slip localization, whether or not damage is taken into account in the non-local variable γ_{cum} , the gradient-enhanced model postpones the onset of average cumulated damage increase.

It becomes apparent that the model is capable of producing brittle and ductile-like evolution of damage. In the case damage is regularized together with slip, the softening and damage occur at lower rate, as expected. A physical interpretation would be that nano-scale cracks extend at a lower rate because of dislocation pile-ups interfering with crack progression, making the material more ductile. Brittle like behavior is observed when regularization is placed on slip alone. In that case, damage resistance decreases drastically faster, because generalized stress effects do not come into play in the cleavage resistance. This can be viewed to be in line with the deformation process zones producing different kinds of failure mechanisms in metallic materials. Further sensitivity analysis on the effect of model parameters is presented in Appendix D.

Grain size affects not only the hardening behavior generated by the model but also the damage onset. It is seen that in the case of smaller grain size (sc. 0.1 mm), damage does not begin to develop at the same time as for the scale of 1.0 mm. Despite the fact that stress levels are larger for the smaller grain size, damage sets on at larger strains than what is observed with larger grains. Certain amount of slip is in fact required to decrease the cleavage resistance and eventually activate damage. Since plastic slip is less localized at grain boundaries and spread more towards the bulk of grains in the smaller scale microstructure, larger macroscopic strains are thus required in order to set damage on.

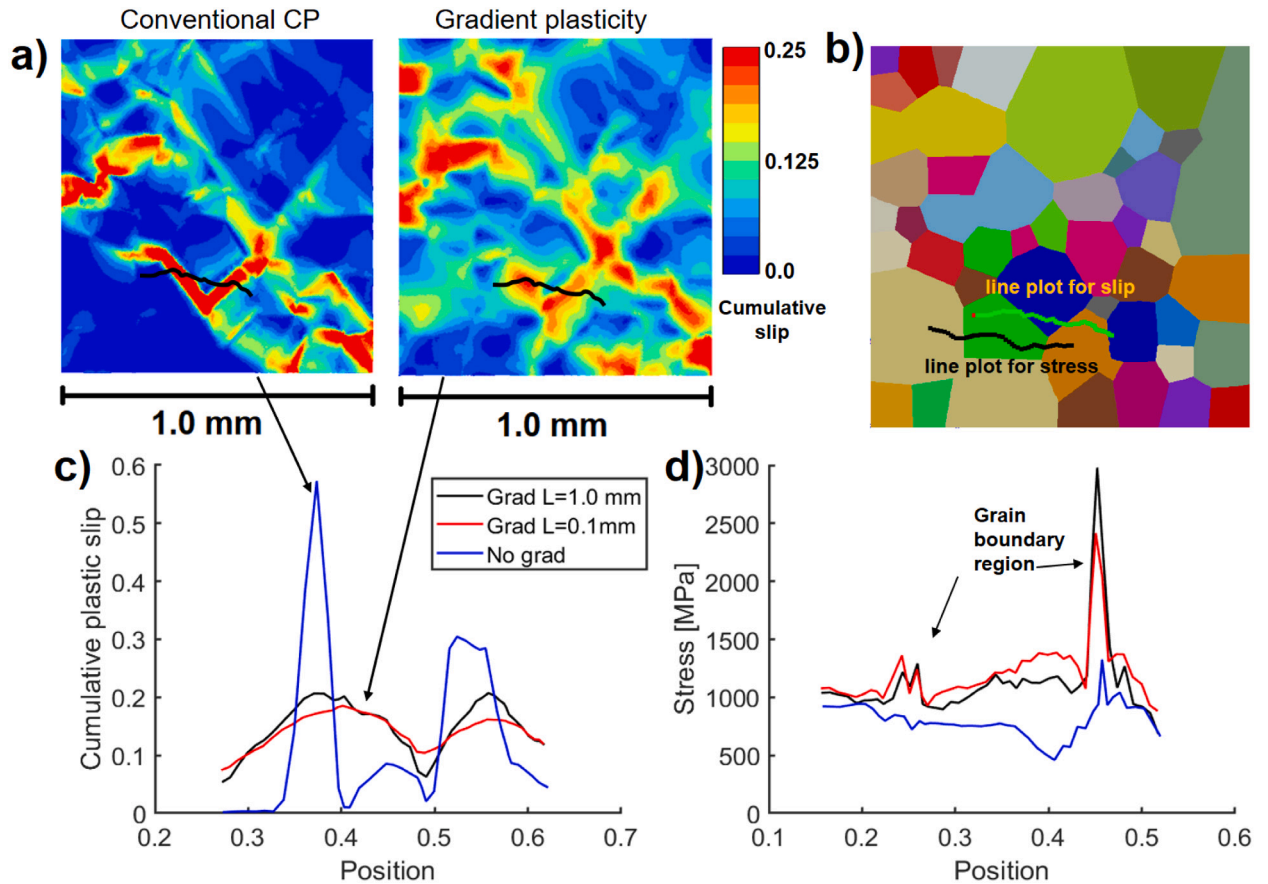


Fig. 8. (a) Plots over predefined path (in black) cumulative plastic slip contours for conventional and strain gradient cases, (b) slip and stress line plots on polycrystalline microstructure, (c) cumulative plastic slip profile, and (d) stress distribution over the line plots. Position coordinates of the gradient case with scaling 0.1 (100 μm) are upscaled 10 times to match normal 1.0 scaling (1000 μm) of the polycrystal aggregate in Figures (c) and (d).

It can be noted that generalized stresses are larger in the vicinity of grain boundaries, since strain gradients are more intense in these regions. It can therefore be argued that models accounting for grain size effects by using a common Hall–Petch (H–P) modification of slip resistance, $\tau_{CRSS}^s = \tau_0 + r^s + K_{HP}/\sqrt{d_g}$ are fundamentally more prone to trigger damage unintentionally earlier. Such an extension indeed does not take into consideration the heterogeneity of slip resistance increase which non-local models predict. However, the common H–P relation could still be used to offset the initial yield for very fine grain sizes with the present model.

The contributions of slip and damage to inelastic strain are further presented in Fig. 10 for slip-only, slip-damage and damage-only regularization. The figure plots only material points of the polycrystalline mesh with non-zero values of damage in order to concentrate on the characteristic of damaged zones. Hence, the probability plot does not include all plastic slip data points, only the ones with non-zero damage. Largest level of cumulative damage are reached when only regularization of slip is considered. In this case, extra hardening introduced by the regularization off-balances the slip-to-damage competition and favors crack growth in spite of the simultaneous softening inflicted to slip resistance by damage. When regularization is placed on both slip and damage, both inelastic strain mechanisms contribute almost equally.

When regularization is placed only on damage in the spirit of Aslan et al. (2011a), slip is highly favored due to strong regularization of damage flow. These observations are visualized in Fig. 11a, b. Plots along a specific path in the mesh, presented in Fig. 11c, d display the smoothening effect of gradient model as well as the biased accumulation of either slip or damage depending on the choice of regularization.

3.4. Application to martensitic microstructures

As an application for the model, tensile simulations were performed on a martensitic microstructure constructed from a scanning electron microscope electron back-scatter diffraction map. Computationally accessible sections intersecting several prior austenite grains and some of their internal blocks and packets are presented in Fig. 12. Three subsections were investigated which correspond to different slices of the material produced by serial sectioning. The section RVEs are discretized to one element thickness. This

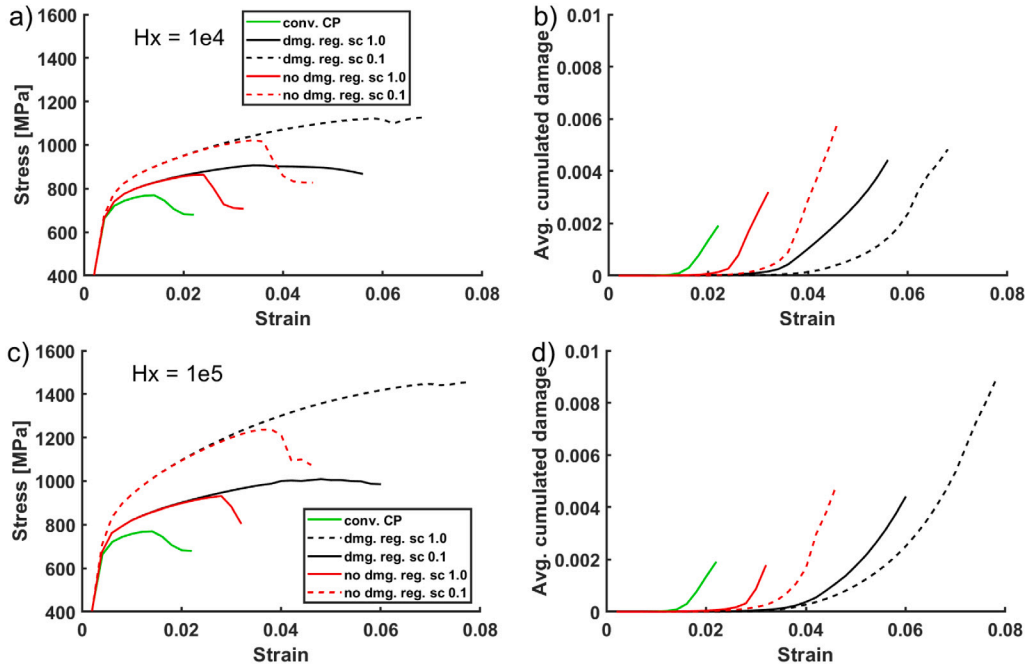


Fig. 9. (a), (c) Stress–strain evolution for two length scales with and without damage regularization, (b), (d) evolution of cumulated damage in a polycrystal, for two H_x values. Aggregate sizes 1.0 and 0.1 mm are referred with sc. 1.0 and sc. 0.1 (scale).

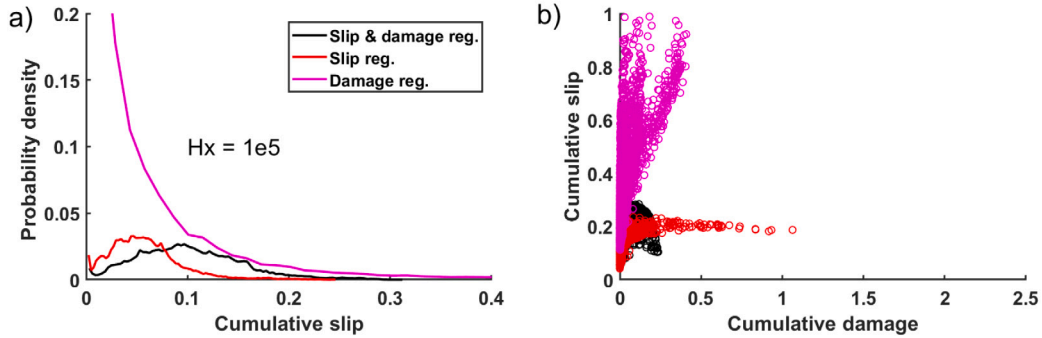


Fig. 10. Distribution of cumulative plastic slip in (a) correlation between cumulative slip and cumulative damage in (b) for material points with non-zero damage at the last step of simulations with different regularization strategies and different values of H_x .

choice essentially provides a limited deformation behavior for a polycrystal, as in-depth grain interaction is not taken into account and in-plane damage is enforced. We provide a preliminary investigation of the slip localization and related damage initiation which was performed up to the level of the ultimate tensile strength and early damage progression, as well as a strategy for parametrization. Regularization is placed on slip alone to avoid excessive limitation of damage growth and overall spread with a single length-scale operator. Furthermore, we exclude the case with only damage regularization, since it does not include length-scale hardening of the microstructure naturally.

The model parameters were first fitted to account for the hardening behavior of steel with a plasticity model without damage on the early part of the stress–strain curve. At the same time, emphasis is placed on replicating the average size of slip localization zones, but not individual slip bands, observed in experiments. The nucleation and evolution of damage was introduced to capture material early cracking and softening behavior near ultimate tensile strength. The next step is the choice of the regularization length, related to the selection of parameter A . This choice amounts to setting the wanted resolution in the simulations with finite width cracks whose thickness is chosen to be sufficiently smaller than the grain size but not too small for computational efficiency. Once the resolution length is set, the remaining damage parameters can be calibrated from the softening part of the tensile curves of the studied material. The procedure is similar to the identification of ductile damage models (Scherer et al., 2021). The parameters used in the simulations with martensite-like meshes that differ from the ones presented in Table 2 are: $\tau_0^s = 190$ MPa, $K = 190$,

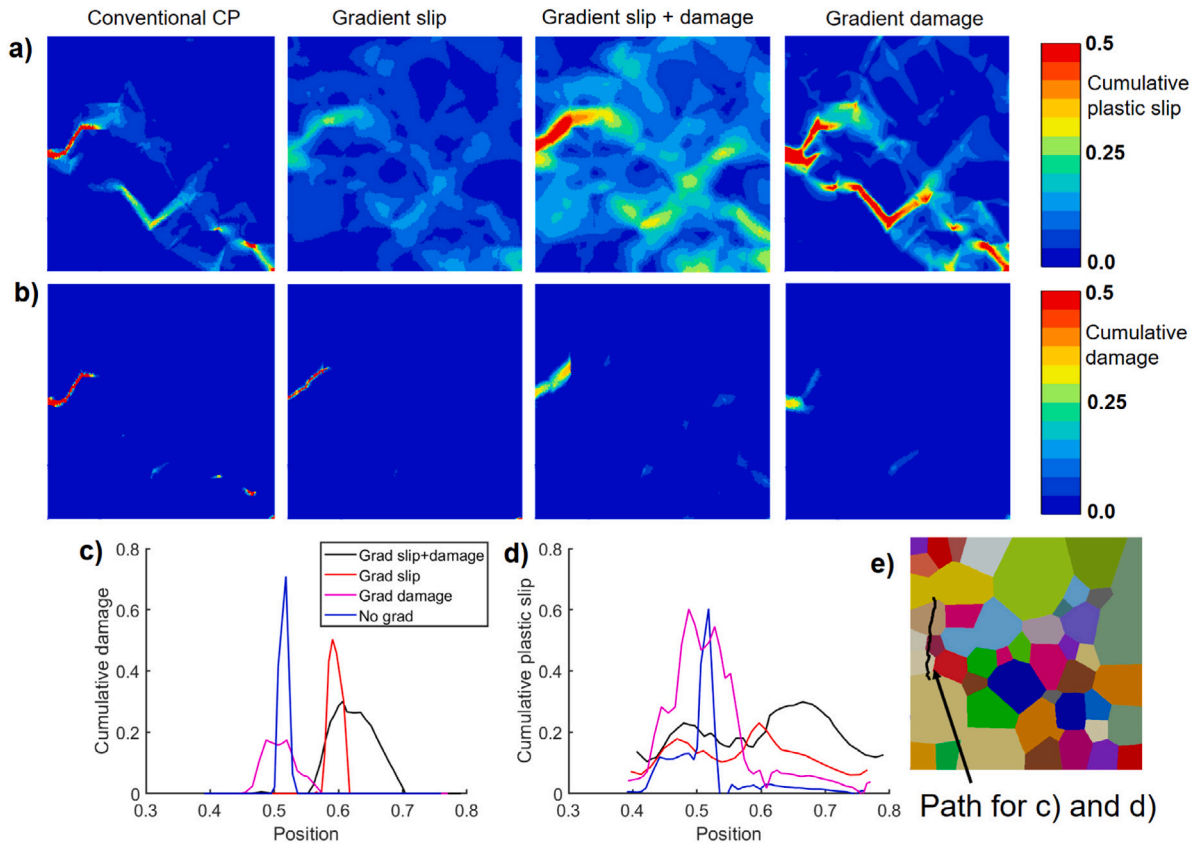


Fig. 11. (a) Slip localization and (b) damage strain during uniaxial tension. Plot over predefined path on damaged region (c) cumulative damage strain, (d) cumulative plastic slip distribution, and (e) prescribed path for position plots on polycrystalline mesh on (c–d). Contours are plotted on undeformed configuration for clarity.

$Q = 7$ MPa, $b = 15$, $\sigma_c^0 = 1350$ MPa, $H = -500$ MPa, $\beta = 1.9$ MPa, $h_1..h_8 = 1.0$, $K_d = 170$, $n_d = 4$. Length scale parameters were set to $H_\chi = 10^4$ MPa and $A = 0.01$ MPa mm².

Fig. 13a, b show simulated stress–strain and cumulative damage curves. Of the chosen microstructures, both microstructure B and C show stronger hardening capability after initial micro-yield due to overall smaller grain size in the subdomain. This is seen in the nominal yield point in the simulations even though that the initial critical resolved shear stress was the same for all simulations. Initiation of damage takes place already around 5% of macroscopic strain. After this incubation period damage increases more rapidly after the ultimate tensile strength observed in the experimental curve. Figs. 13c, d illustrate the fields of cumulative plastic slip, cleavage resistance and cumulative damage in the microstructures A and C. Both show a significant plastic strain localization within 10 μ m region, which was also observed in the experiments illustrated in Fig. 13e. This shear concentrated region includes several grains. Due to the chosen coupling between damage and slip and related decrease in cleavage resistance, damage tends to occur mainly within the slip rich region. Intense damage can be observed to select both intra-granular and grain boundary type damage mechanisms. This essentially depends on the local grain orientation, susceptibility to intra-grain strain localization, and stress concentrations arising from grain-to-grain interactions.

The present preliminary simulations imply that a parametric set capable of describing macroscopic stress–strain curve is obtainable. However, a more quantitative verification would be necessary to verify the strain fields with in-situ digital image correlation methodology on the present material to address the model’s local capability to present or suppress strain localization, such as suggested by Zouaghi et al. (2016). This is one future item of work. For initial evaluation, Fig. 13c show strain patterning on the surface of a small scale tensile sample deformed inside SEM. It was observed that slip localization precedes damage formation, as found in the simulations. However, the observations from the experiment was not sufficient to quantify slip-to-damage causality and the identification of damage (fine scale cracks) is not straightforward based only on imaging of the surface deformation. It is desired to identify the relation of preceding slip localization to damage to establish coupling between the mechanisms. The resulting damage scattering with slip and damage regularization suggests, that separation of length-scales related to slip and damage might be necessary too, since the present approach rudimentary involves slip and damage under one regularization variable due to computational robustness.

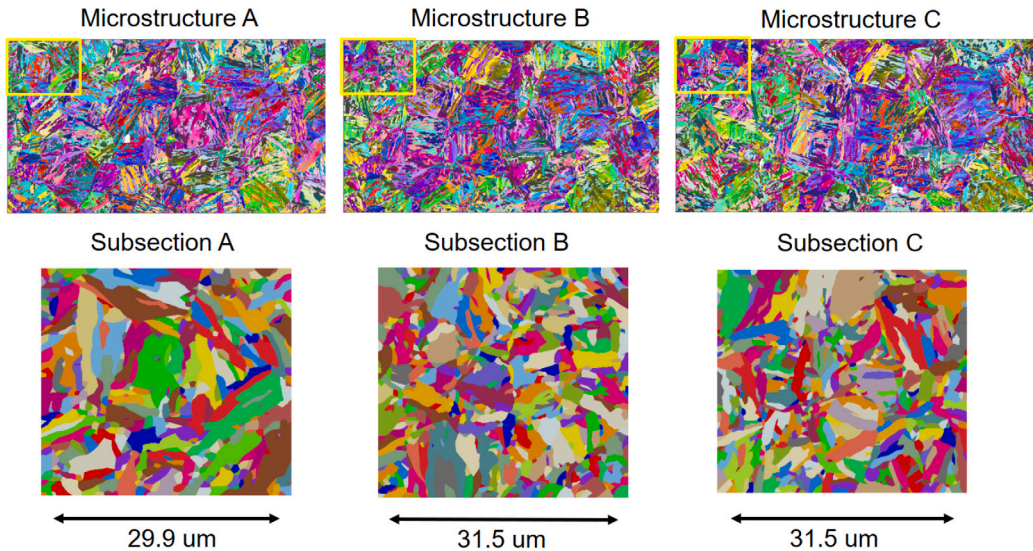


Fig. 12. Three computational microstructures sub-sectioned from different EBSD measurements.

4. Discussion

4.1. Scaling effects

Modern advanced steels set aim to extreme strength and ductility. One key aspect of reaching this goal is the refinement of grain size and modification of grain morphologies, and enhancing the effect of hierarchical strengthening mechanisms (arising from, e.g., martensite and bainite size, and nano-scale twins), assisted by secondary phases such as fine austenite intra-lath films, retained austenite as well as precipitates and carbides. Furthermore, the local strains can become large and plastic gradients may easily develop for such complex microstructure, especially when the material is imperfect for example with voids, cracks, inclusions, secondary soft and hard phases. Thus, the material design challenge of how to provide better properties is certainly not trivial. These aspects readily justify the need for length-scale dependent analysis tools operating at microstructural level from the strengthening point of view and up to evolution based damage presentations, for which the present investigation provides a reasonable initial perspective. It should be noted that detailed analysis of strengthening mechanisms related to GNDs, slip or kink bands, might further benefit of more elaborate generalized continuum methods (Forest, 2009; Chang et al., 2016), instead of a single cumulative variable contributed by all slip systems and possibly damage.

Nonetheless, finite sized slip bands and bundles, kink bands, and related size effects are necessary to be considered in materials operating at very fine effective grain sizes in general, whether their formation is controlled with the reduced (current) or full model (Rys et al., 2020; Chang et al., 2016). The present method aims to remain computationally efficient, provide sufficient regularization effects and give a tractable basis for further development and incorporation of features of generalized continua, all in a finite strain formalism.

To this effect, Cordero et al. (2013) and Chang et al. (2016) observed a wide scaling capability for a micromorphic based crystal plasticity model, that can achieve extended scaling law exponents m from 0 to -2 ($\Delta\sigma \propto d^m$), in addition to conventional Hall–Petch like grain size exponent of -0.5 . This model called *microcurl* utilizes the full curl of the plasticity deformation tensor, which can be related to dislocation density allowing interpretation of geometrically necessary dislocations (Rys et al., 2020; Chang et al., 2016). For the *microcurl* model and the present case, the scaling effects can be rationalized and related to characteristic length scale ℓ_c , which has a dependency on two generalized moduli H_χ and A so that $\ell_c = \sqrt{A/H_\chi}$ (Cordero et al., 2013). The control over the parametrization allows to achieve different *tanh*-shaped scaling curves with respect to effective grain size, which was observed in Fig. 6 and in Fig. A.16 in Appendix A.

4.2. Choice of regularization method

In micromorphic crystal plasticity without damage, the higher order modulus A relating the higher order stress to the gradient of the micromorphic variable has a physical meaning which is related typically to the characteristic size of dislocation pile-ups at obstacles like phase and grain boundaries, e.g., as discussed in Forest and Sedláček (2003) for dislocation based estimates for A . However, when the micromorphic approach is applied to damage phenomena in single crystals, as initially proposed by Aslan et al. (2011a) the physical meaning is somewhat lost since the model is used for the purpose of regularization of the damage model. In that case, the characteristic length associated with A sets a minimal resolution for the simulation, and the meaning is related to a

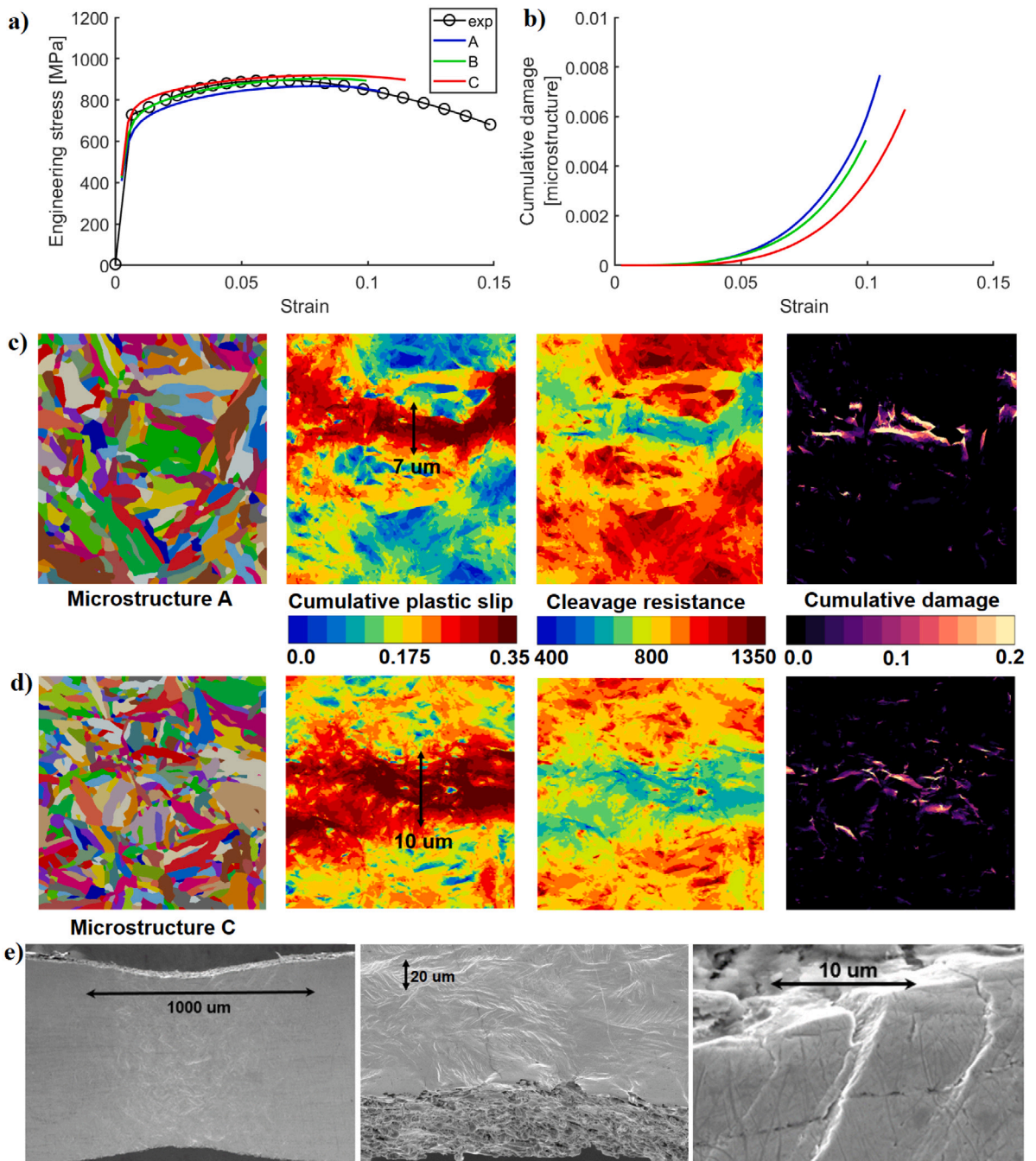


Fig. 13. (a) Experimental and simulated stress–strain curves, (b) simulated cumulative damage over the whole microstructure, (c) and (d) microstructure, cumulative plastic, effective cleavage resistance, and cumulative damage for microstructures A ($\epsilon = 10.5\%$) and C ($\epsilon = 11.5\%$), respectively. (e) SEM characterization of a small-scale tensile specimen with strain localization and cracking.

modeling choice, discussed below. Events taking place at a smaller scale are smeared out. This resolution can be phenomenologically related to the typical size of the damaged zone along the crack path. In the present work, the micromorphic approach was used for regularization purposes.

It is found that the choice of model framework related to regularization of inelastic flow is not necessarily unique. In many cases, the decision is driven by the need to introduce length-scale driven extra-hardening and control of slip localization phenomenon. In addition, the regularization of crack like behavior as damage is an object of special interest when crack growth is considered in heterogeneous materials such as martensite. The model results showed that regularization placed on slip alone is capable of

introducing length-scale relevant hardening and undertake necessary regularization of slip localization that indirectly affects damage behavior. This is an outcome of how the model couples damage and plasticity, however, the magnitude of this effect is much dependent on chosen parametrization as shown in Fig. D.22.

The second option to regularize both slip and damage allows the control of slip band formation in the first place and then the extra-hardening stabilizes damage rate and produces more bounded strain localization sites and damage bands. This was clearly observed in Figs. 9 and 11. There is, however, a vital restriction with this alternative. If damage is taken to crack the material successfully and the crack is open, regularization should no longer be applied to avoid unrealistic hardening behavior of non-intact material regions. The same restriction exists in cyclic fatigue conditions under which the model allows smeared crack closure. Thus, one of its main advantage relies with the desired control of damage band width. The main restriction then exists with the slip bands themselves. They are not effectively regularized and the extra-hardening related to plasticity, and its inherent capability to provide grain size related scaling vanishes. As a result it is not possible to associate distinct length scales for the plasticity and damage phenomena, which can be seen as a drawback of the formulation. If necessary, it is however possible to consider two gradient contributions with two distinct length scales. This was not attempted in the present work as pointed out.

4.3. Slip and damage in single and polycrystals

The single crystal analyses showed that spurious mesh dependency related to softening with damage is reduced greatly or disappearing when compared to conventional crystal plasticity approach. This is one of the key objectives of the model. Another aspect is that the model is anisotropic since it considers specific crystallographic planes for cleavage, which is in contrast to a variety of recent polycrystal models which mainly rely on isotropic damage formulations (Mareau, 2020). The model contains a single characteristic length parameter, A , corresponding to isotropic or cubic gradient contribution, however, again the damage model itself is strongly anisotropic.

As pointed out, the diffusivity or concentration of damaged bands can be controlled with a suitable parametrization. Besides, the length-scale hardening occurring in the polycrystalline structure and the constrained widening of damaged bands affect the failure predictions. Importantly, the single crystal results also show that defect (e.g. pores) induced slip and damage banding remains finite sized. Prediction of initiation of failure process depends largely on the smoothening subjected to slip. Therefore, the meaning of diffuse slip bands is mostly damage delaying and scattering. In contrast, the high stresses produced at grain boundaries by using high penalty factors together with concentrated slip flow, are a source promoting damage in the present model. This not only allows the intra-grain level damage, but also allows the interfacial damage to occur naturally in the model because of the projection of opening stress at cleavage planes. Characteristic martensite length-scales with relation to hardening and damage can be investigated with the model but careful quantification should be performed in future. Importantly, the guided length-scale saturation is a critical perk in terms of generating realistic damage patterning. The main advantage of the presented model is that it includes the possibility of accounting for cleavage cracking in polycrystals in combination with usual crystal plasticity.

5. Future work

An interesting future topic for lath martensitic steel is to introduce 3D tomography reconstructed models having defects, such as inclusions with realistic geometries, local microstructure (matrix and defect), and interfaces, to have a view on the effect of defects to damage evolution. With proper higher order description of the present model together with a detailed microstructure, it is possible to investigate relations between lath martensite matrix hierarchies and strengthening and size effects related to a specific 3D geometry of the inclusions regarding susceptibility to damage. The objective of this work was not to utilize dislocation density based formulation, however, it remains as an alternative to the currently proposed constitutive equations. Furthermore, a comparison of the cleavage-based damage model used in this work, and the porosity-based single crystal ductile failure model developed in Han et al. (2013), Ling et al. (2016) could also be envisaged.

The micromorphic model presented in this work can be computationally demanding when large scale simulations are envisaged. The main reason of such a feature lies in the necessity to use a large penalty modulus H_γ in order to ensure quasi-equality between γ_{cum} and γ_χ . Given that it is combined with a quasi rate-independent viscoplastic formulation of crystal plasticity (i.e. a large viscous exponent n) time-integration of the resulting stiff constitutive equations requires small time steps to be performed. In order to alleviate such difficulties a non-local formulation based on a Lagrange multiplier approach as in Zhang et al. (2018) could be applied. Scherer et al. (2020) recently followed this path and compared the computational efficiency of micromorphic and Lagrangian approaches for rate-independent and viscoplastic crystal plasticity settings.

6. Conclusions

The main outcomes of the work are the following:

- Reduced micromorphic crystal plasticity model produces size dependent scaling and bounded *tanh*-type hardening with respect to grain size produced by the regularization power of the model. Extra strain-hardening is observed near the grain boundaries and at strain localization sites. Decreasing grain size and its relation to model's characteristic length-scale introduce spreading of strengthening, with a similar phenomenological characteristic to geometrically necessary dislocation assisted hardening. Similar hardening behavior is achievable with the *microcurl*-model (Cordero et al., 2013), making the reduced model very attractive as a computationally efficient alternative.

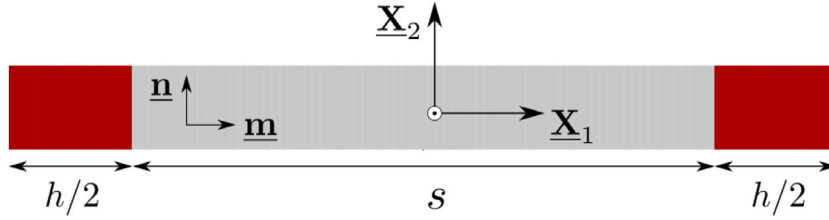


Fig. A.14. Periodic two phase laminate geometry with the soft phase (gray) of width s undergoing elasto-plastic deformations with a single slip system ($\underline{n}, \underline{m}$) and the hard phase (red) of width h undergoing purely elastic deformations. (For interpretation of the references to color in this figure legend, the reader is referred to the web version of this article.)

- Different regularization techniques subjected to dislocation slip and crystalline level damage were investigated. Main advantage of the model with damage is the capability to produce regularized cleavage damage. Scaling effects can be introduced in the model by the control of slip band evolution with the regulated slip flow rule. This choice leads to indirect coupling between slip and indirectly regulated damage, since slip regularization affects the width of zones susceptible to damage through the plasticity-damage constitutive coupling. When a single micromorphic inelastic microstrain variable is contributed by both slip and damage mechanisms, the length-scale effects are observed and the damage evolution is more regulated and smoothed. Excessive damage regularization should be avoided, when the material is completely fractured to avoid unrealistic hardening.
- The reduced micromorphic approach allows for analyzing of microscale deformation and damage phenomena in martensitic steels. An advantage of the model is the capability to generate size dependent hardening with proper higher order conditions at the hierarchical packet/block/lath and grain boundaries. Shear banding phenomenon can be controlled with regularization and damage initiation is dependent on length-scale hardening and shear band formation. Model parametrization is adjustable to generate brittle or quasi-brittle type of fracture in martensitic microstructures related to shear bands or scattering of damage, depending on characteristics of failure evolution in the material. Predictions of tensile failure with the model depend mainly on the scaling effects (grain size, slip localization), material tendency to cleavage fracture (atomistic setting and defect population), and non-local evolution of damage and its spreading (regularization, diffuse/localized and microstructural scattering), all included in the same model concept.

Declaration of competing interest

The authors declare that they have no known competing financial interests or personal relationships that could have appeared to influence the work reported in this paper.

Acknowledgments

The authors would like to acknowledge the financial support of Business Finland in the form of a research projects ISA Wärttilä Dnro 7734/31/2018 and ISA VTT Dnro 7980/31/2018. Matti Lindroos has received funding from the Euratom research and training programme 2019–2020 under grant agreement No 900018 (ENTENTE project) related to the model development of this work. Tomi Suhonen is acknowledged for providing in-situ SEM tensile test data and SEM images for analysis.

Appendix A. Two-phase laminate without damage

Following Forest (2008), Cordero et al. (2010) and Aslan et al. (2011a), the behavior of a periodic two-phase single crystal laminate under a macroscopic shear loading is investigated. The periodic microstructure is sketched in Fig. A.14 where a hard phase (h) is colored in red and a soft phase (s) is colored in gray. The hard phase is purely elastic, while the soft phase can undergo elasto-plastic deformations. In the soft phase, plastic slip can occur only in a single slip system composed of the normal to slip plane \underline{n} and slip direction \underline{m} . We consider a linear hardening behavior of the soft phase such that $\tau_c = \tau_0 + H_0\gamma$, where H_0 is a positive linear hardening modulus. A macroscopic shear deformation $\bar{\gamma}$ is applied in the crystal slip direction. The following displacements and micro-slip fields $\underline{u}(\underline{X})$ and $\gamma_\chi(\underline{X})$ are considered

$$u_1 = \bar{\gamma}x_2 \quad u_2 = u_2(x_1) \quad u_3 = 0 \quad \gamma_\chi = \gamma_\chi(x_1) \quad (\text{A.1})$$

In the context of finite deformations and with the assumption of small elastic deformations this results in

$$\underline{\mathbf{F}} = \begin{pmatrix} 1 & \bar{\gamma} & 0 \\ u_{2,1} & 1 & 0 \\ 0 & 0 & 1 \end{pmatrix}, \quad \underline{\mathbf{F}}^i = \begin{pmatrix} 1 & \gamma & 0 \\ 0 & 1 & 0 \\ 0 & 0 & 1 \end{pmatrix} \quad (\text{A.2})$$

$$\underline{\mathbf{E}}_{GL}^e = \frac{1}{2} (\underline{\mathbf{F}}^{eT} \cdot \underline{\mathbf{F}}^e - \underline{\mathbf{1}}) \approx \frac{1}{2} \begin{pmatrix} 0 & (\bar{\gamma} - \gamma) + u_{2,1} & 0 \\ (\bar{\gamma} - \gamma) + u_{2,1} & 0 & 0 \\ 0 & 0 & 0 \end{pmatrix} \quad (\text{A.3})$$

From Eq. (16) and assumption of small elastic deformations one also obtains $\underline{\Pi}^M \simeq \underline{\Pi}^e$ and therefore

$$\begin{aligned} \tau &= \underline{\Pi}^M : (\underline{m} \otimes \underline{n}) \simeq \underline{\Pi}^e : (\underline{m} \otimes \underline{n}) \\ &= \Pi_{12}^e = 2C_{44}E_{GL,12}^e = C_{44}(\bar{\gamma} - \gamma + u_{2,1}) \end{aligned} \quad (\text{A.4})$$

where C_{44} refers to the shear modulus. The balance Eq. (9) imposes Π_{12}^e to be uniform across the laminate and thus also τ . Combining Eq. (10), (20) and (21) yields the second order partial differential equation

$$A\gamma_{\chi,11} = H_{\chi}(\gamma_{\chi} - \gamma) \quad (\text{A.5})$$

Upon neglecting viscous stresses one has from the yield condition in the soft phase

$$\tau + S = \tau_0 + H_0\gamma \quad (\text{A.6})$$

It follows that Eq. (A.5), in the soft phase (superscript s), is an hyperbolic linear in-homogeneous differential equation

$$\gamma_{\chi,11}^s - (\omega^s)^2 \gamma_{\chi}^s + (\omega^s)^2 \frac{\tau - \tau_0}{H_0} = 0, \quad \omega^s = \sqrt{\frac{H_0 H_{\chi}^s}{A^s (H_0 + H_{\chi}^s)}} \quad (\text{A.7})$$

$1/\omega^s$ represents the characteristic length of the material in the soft phase. In the hard phase (superscript h) $\gamma = 0$ and Eq. (A.5) simply becomes an hyperbolic linear homogeneous second order differential equation

$$\gamma_{\chi,11}^h - (\omega^h)^2 \gamma_{\chi}^h = 0, \quad \omega^h = \sqrt{\frac{H_{\chi}^h}{A^h}} \quad (\text{A.8})$$

$1/\omega^h$ represents the characteristic length of the material in the hard phase. Eq. (A.7) and (A.8) can be solved analytically and separately in order to obtain the form of the profile in the whole periodic microstructure. One obtains an hyperbolic profile in each phase such that

$$\gamma_{\chi}(x_1) = \begin{cases} C^s \cosh(\omega^s x_1) + D & x_1 \in \left[-\frac{s}{2}; \frac{s}{2}\right] \\ C^h \cosh\left(\omega^h \left(x_1 \mp \frac{s+h}{2}\right)\right) & \pm x_1 \in \left[\frac{s}{2}; \frac{s+h}{2}\right] \end{cases} \quad (\text{A.9})$$

where the symmetry condition $\gamma_{\chi}(-x_1) = \gamma_{\chi}(x_1)$ was used. Interestingly, exactly the same form of solution is found for the scalar micro-slip variable γ_{χ} as the one developed for the microdeformation component χ_{12} by Aslan et al. (2011a). To that extent the present model can be seen as a degenerate formulation of the so-called *microcurl* model. Although plastic slip is inactive in the hard elastic phase, the micro-slip variable does not vanish in this phase. This attribute is imposed by continuity of the higher order stress traction M_1 at the interfaces. As explained by Cordero et al. (2010) this feature is essential to trigger size effects. The coefficients C^s , D and C^h are integration constants which can be determined by considering interfaces and periodicity conditions.

- Continuity of γ_{χ} at the interfaces ($x_1 = \pm s/2$)

$$C^s \cosh\left(\omega^s \frac{s}{2}\right) + D = C^h \cosh\left(\omega^h \frac{s}{2}\right) \quad (\text{A.10})$$

- Continuity of the higher order traction M_1 at the interfaces ($x_1 = \pm s/2$)

$$C^s \omega^s \sinh\left(\omega^s \frac{s}{2}\right) = -C^h \omega^h \sinh\left(\omega^h \frac{s}{2}\right) \quad (\text{A.11})$$

- Periodicity of the displacement component u_2 .

Recalling Eq. (A.4), the yield condition in the soft phase Eq. (A.6) and $\gamma = 0$ in the hard phase it comes

$$u_{2,1} = \begin{cases} \frac{\tau_0}{C_{44}} - \bar{\gamma} + \frac{A^s \omega^s C^s}{H_0} \cosh(\omega^s x_1) + \frac{H_0 + C_{44}}{C_{44}} D & x_1 \in \left[-\frac{s}{2}; \frac{s}{2}\right] \\ \frac{\tau_0}{C_{44}} - \bar{\gamma} + \frac{H_0}{C_{44}} D & \pm x_1 \in \left[\frac{s}{2}; \frac{s+h}{2}\right] \end{cases} \quad (\text{A.12})$$

Periodicity of u_2 enforces the average of $u_{2,1}$ over the whole laminate to vanish. Therefore, introducing the microstructure length $\ell = s + h$, one obtains

$$\left(\frac{\tau_0}{C_{44}} - \bar{\gamma}\right) \ell + \frac{2A^s \omega^s C^s}{H_0} \sinh\left(\omega^s \frac{s}{2}\right) + \frac{H_0 \ell + C_{44} s}{C_{44}} D = 0 \quad (\text{A.13})$$

We introduce the soft phase fraction $f_s = s/\ell$. The yield condition in the soft phase (A.6) allows to derive the macroscopic (mean) stress $\bar{\Pi}_{12}^e$

$$\bar{\Pi}_{12}^e = \int_{-\frac{\ell}{2}}^{\frac{\ell}{2}} \tau dX_1 = \tau_0 + \frac{H_0}{f_s} \langle \gamma \rangle - \frac{A^s}{f_s} \langle \gamma_{\chi,11}^s \rangle = \tau_0 + H_0 D \quad (\text{A.14})$$

where it was used according to (A.5) that $\langle \gamma \rangle = \left\langle \gamma_{\chi}^s - (A^s/H_{\chi}^s) \gamma_{\chi,11}^s \right\rangle$. From the latter it also follows from (A.9)

$$\langle \gamma \rangle = \frac{2A^s \omega^s C^s}{H_0 \ell} \sinh\left(\omega^s \frac{f_s \ell}{2}\right) + f_s D \quad (\text{A.15})$$

Table A.3

Set of material parameters used in the single slip analytical resolution and finite element simulations in accordance with Aslan et al. (2011a).

Phase	μ [MPa]	τ_0 [MPa]	H [MPa]	H_χ [MPa]	A [MPa mm ²]
Soft (s)	35,000	40	5000	5×10^5	1×10^{-3}
Hard (h)	35,000	–	–	5×10^5	5×10^{-5}

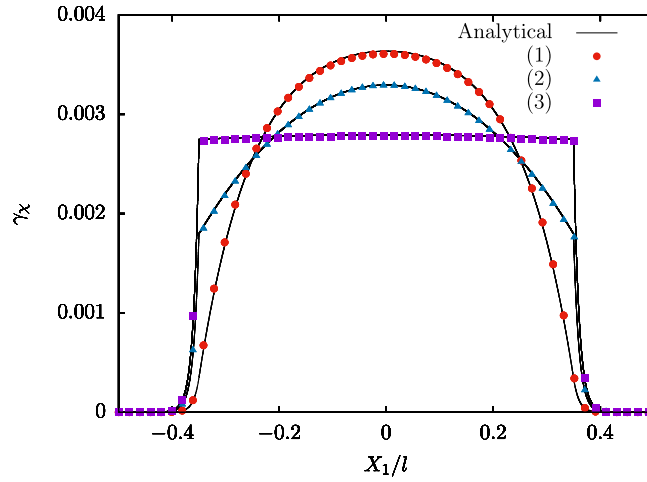


Fig. A.15. Analytical (solid lines) and numerically computed (colored dots) profiles of micro-slip in the periodic two-phase laminate at 0.2% macroscopic shear strain obtained with the micromorphic model with material parameters presented in Table A.3. (1) in absence of mismatch of the characteristic length between the two phases $A^s = A^h = 5 \times 10^{-5}$ MPa mm², (2) an intermediate mismatch between the two phases $A^s = 1 \times 10^{-3}$ MPa mm² and $A^h = 5 \times 10^{-5}$ MPa mm², (3) a stronger mismatch between the two phases $A^s = 5 \times 10^{-2}$ MPa mm² and $A^h = 5 \times 10^{-5}$ MPa mm². The fraction of soft phase is $f_s = 0.7$ and the microstructure size $\ell = 1 \mu\text{m}$.

Introducing the constant κ as

$$\kappa = \frac{\coth\left(\omega^s \frac{f_s \ell}{2}\right)}{A^s \omega^s} + \frac{\coth\left(\omega^h \frac{(1-f_s)\ell}{2}\right)}{A^h \omega^h} \tag{A.16}$$

from Eq. (A.10), (A.11) and (A.15) one identifies the integration constants involved in (A.9)

$$C^s = -\langle \gamma \rangle \left[A^s \omega^s \sinh\left(\omega^s \frac{f_s \ell}{2}\right) \left(f_s \kappa - \frac{2H_0}{\ell} \right) \right]^{-1} \tag{A.17}$$

$$D = \langle \gamma \rangle \left[f_s - \frac{2}{H_0 \ell \kappa} \right]^{-1} \tag{A.18}$$

$$C^h = \langle \gamma \rangle \left[A^h \omega^h \sinh\left(\omega^h \frac{(1-f_s)\ell}{2}\right) \left(f_s \kappa - \frac{2H_0}{\ell} \right) \right]^{-1} \tag{A.19}$$

Fig. A.15 plots the analytical and numerically computed micro-slip profiles obtained for three different couples (A^h, A^s) and other material parameters, taken from Aslan et al. (2011a), are presented in Table A.3. The penalization moduli are taken equal in both phases $H_\chi = H^s = H^h$ and the fraction of soft phase is chosen as $f_s = 0.7$. The numerical solutions (solid lines) obtained by finite element analysis fit very well the analytical solutions and are also in agreement with the solutions found in Aslan et al. (2011a). For a small characteristic length of the soft phase, non-negligible gradients can exist in the microstructure and thus the micro-slip profile appears rounded (red circles). As the characteristic length increases, gradients of micro-slip tend to vanish resulting in an almost flat profile in the soft phase. Continuity of γ_χ and non-vanishing values in the elastic phase are unfailingly observed as expected.

Fig. A.16 plots the evolution of the macroscopic stress $\overline{\Pi}_{12}^e$ at 0.2% overall shear deformation obtained from Eq. (A.14) as a function of the microstructure length ℓ . Several values of the penalty parameter $H_\chi (= H^s = H^h)$ are used and other material parameters are presented in Table A.3. For large microstructure no significant size effects are observed and H_χ plays almost no role on the macroscopic shear stress. Nevertheless as the microstructure size decreases size effects become substantial and the effect of H_χ becomes paramount. The effect of H_χ pertains two major aspects. First, in the log-log plot of Fig. A.16 the slope of the scaling law at intermediate microstructure length becomes steeper as H_χ increases. In addition, the saturation value of $\overline{\Pi}_{12}^e|_{0.2}$ for small microstructures increases with H_χ . All in all H_χ induces jointly a more sensitive dependence to the microstructure size and more important size effects.

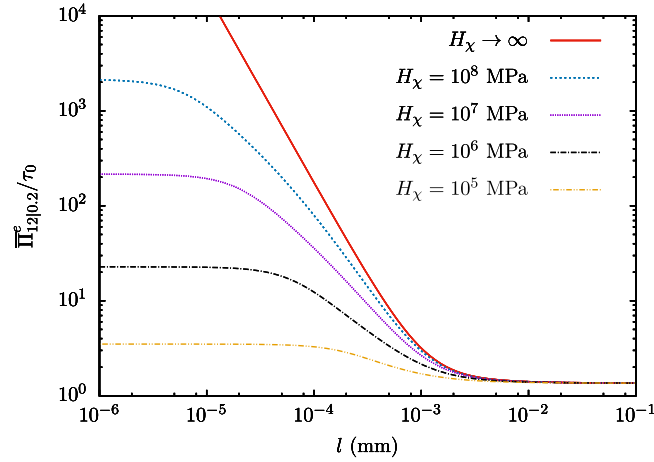


Fig. A.16. Evolution of the normalized macroscopic stress $\bar{\Pi}_{12|0.2}^e / \tau_0$ at 0.2% macroscopic shear strain as a function of the microstructure length l for several values of the penalization parameter H_χ with $f_s = 0.7$ and material parameters presented in Table A.3.

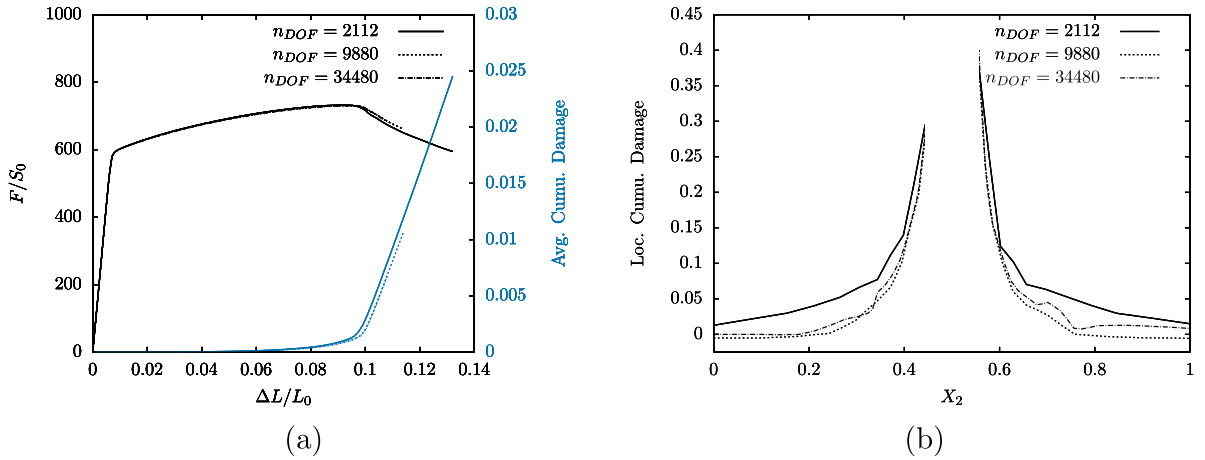


Fig. B.17. Mesh size convergence analysis on [100]–[010]–[001] crystal orientation in terms of (a) macroscopic stress–strain and average cumulated damage measures and (b) local cumulated damage at $\Delta L/L_0 = 0.1$ when acceleration of average cumulated damage sets on. H_χ is set to 10^4 MPa. (For interpretation of the references to color in this figure legend, the reader is referred to the web version of this article.)

Appendix B. Convergence with respect to mesh size

In order to demonstrate the regularization capability of the single crystal damage model, when both slip and damage are accounted for regularization (see Eq. (4)), three mesh densities are considered. The convergence with respect to mesh size was also verified for the two other formulations (see Eq. (4) or Eq. (6)), but results are not reported here for conciseness. Meshes used for mesh density convergence validation are composed of 80, 400 and 1440 elements and respectively possess 2112, 9880 and 34480 degrees of freedom. Mesh convergence analysis is performed on a BCC single crystal with crystal axes [100], [010] and [001] initially respectively aligned with the basis vectors. Fig. B.17(a) shows the engineering stress–strain curves (black) and volume average cumulated damage curves (blue) obtained with the different mesh densities. It can be noted that before acceleration of average cumulated damage (strains lower than ~ 0.1) all meshes result in identical predictions in terms of stress and average cumulated damage. The onset of acceleration of average cumulated damage, and corresponding stress drop, is slightly anticipated with the coarsest mesh. However, from the results obtained with the two most refined meshes it is clear that mesh convergence, in terms of macroscopic measures, is attained. In Fig. B.17(b) are plotted, at $\Delta L/L_0 = 0.1$, the local values of cumulated damage along the blue line (where damage localizes because of the load-bearing section reduction due to the void) depicted in Fig. 1. It can be observed that the coarsest mesh predicts the largest value of local cumulated damage over the whole profile line. In contrast the two most refined meshes produce less intense and rather close local cumulated damage profiles. Far from the highly damaged zone some discrepancies can be observed in terms of local cumulated damage. However, in the vicinity of the void, where damage is intense both most refined meshes are in agreement.

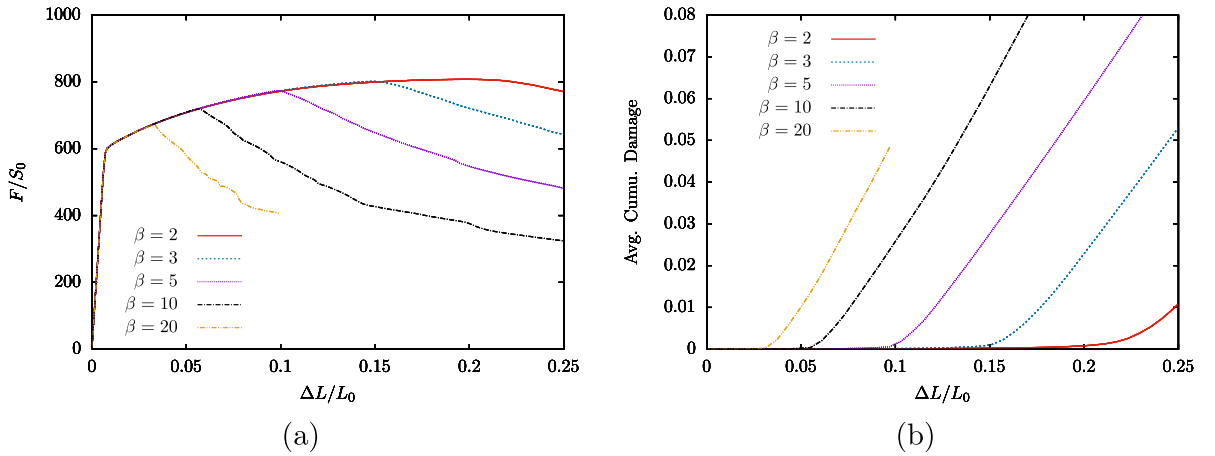


Fig. C.18. Influence of parameter β on (a) the stress–strain behavior and (b) average cumulated damage evolution for a [100]–[010]–[001] crystal orientation with $H_\gamma = 10^4$ MPa.

Appendix C. Influence of material parameters β and H

Influence of the coupling parameter β in Eq. (28) and (32) is assessed. This parameter scales the relation between damage and critical resolved shear stress driven softening. The larger β is, the more softening induced by damage there is. Furthermore, larger values of β also make damage and slip resistance to decrease faster. Nevertheless β only plays a role on the slip resistance once damage is activated. These observations appear clearly in Fig. C.18 where several values of β ranging between 2 and 20 were used. It can be noticed indeed that prior to onset of damage all curves are identical regardless of the value of β . However damage sets on earlier with the largest β value since the damage resistance has decreased more rapidly. The computation with largest value of β also predicts a rapid acceleration of average cumulated damage which is accompanied by an early macroscopic stress drop. On the contrary the lowest value of β postpones onset of damage, because the slip resistance decreases slowly. In addition the increase of average cumulated damage and thus the softening part of the stress–strain curve are delayed. It appears that β can hence be used as a scaling parameter that settles the local strain at which damage will start to occur and how it will affect acceleration of slip resistance drop provoking final failure.

The additional term Hd is added in Eq. (32) in order to accelerate the decline of damage resistance. This triggers apparition of localization of damage into crack-like zone as noted in Aslan et al. (2011a). Influence of the linear modulus H is analyzed and presented in Fig. C.19 which displays macroscopic stress–strain and average cumulative damage curves obtained with $H \in \{10^3; 10^4\}$ MPa. On the macroscopic stress–strain behavior the main effect of H is to step up the softening rate. When H is increased a sharper drop of the stress is predicted. At local level a larger value of H induces a faster reduction of slip resistance and as feedback damage increases faster. This results in an early rise of average cumulated damage. As a collateral effect softening occurs slightly earlier on the macroscopic stress–strain curve. A side effect of the rapid acceleration of softening when a large value of H is used is that damage becomes more localized. This is discernable on damage fields but also evidenced on the average cumulated curves where a flattening of damage augmentation can be observed for the largest H values.

Appendix D. Effect of strain gradient and damage parametrization

Plasticity and damage evolution in the model are contributed by several plasticity and damage related parameters. The following analysis assesses the phenomena originating from different parametrizations in polycrystals, either related to the strain-gradient and plasticity-damage parts. Generalized moduli H_γ and A grant the scale-dependency in the model that influences primarily slip localization and the following damage. Furthermore, the explicit constitutive relations placed on coupling of plasticity and damage imposes direct interaction between the two mechanisms of inelastic strain in the model. It follows that regularization further affects the coupling directly or indirectly as previously observed in Fig. 10.

Fig. D.20 shows the effect of three values of penalty modulus H_γ . The characteristic length scale ℓ_c also changes when the value of H_γ increases in addition to the actual changes in grain size related scaling exponent, given that A is set constant. A polycrystal microstructure shown in Fig. 7a was used in the simulations. Damage band shape and magnitude in Fig. D.20c suggest that the penalization caused by $H_\gamma = 10^4$ MPa does not yet reach the saturation like behavior of the greater H_γ values, confirming the single crystal results. The two higher H_γ values produce very similar damage bands, which in turn indicates that $H_\gamma = 10^5$ MPa generally suffices as a penalty term value for slip and damage regulated flow.

It is characteristic for reduced micromorphic model that, increasing value of the higher order modulus A widens the effective slip band width and reduces cumulative slip absolute magnitude, when modulus A is constant (Ling et al., 2018b; Scherer et al., 2019). At the same time, spreading of the extra-hardening affected zone occurs at the microstructure level in conjunction with grain–grain

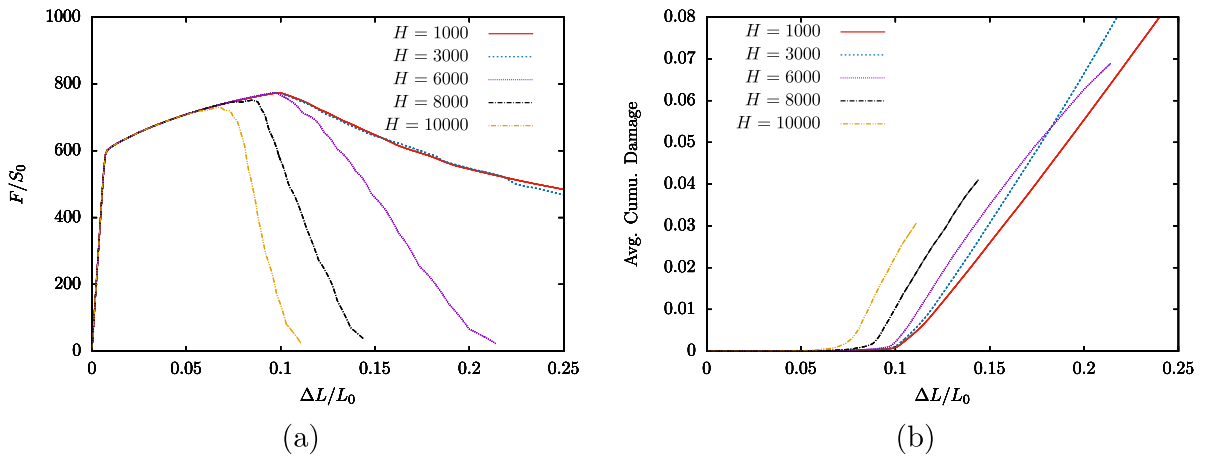


Fig. C.19. Influence of parameter H on damage onset and softening acceleration for $[100] - [010] - [001]$ crystal orientation with $H_x = 10^4$ MPa. Parameter H is treated as negative value to cause softening.

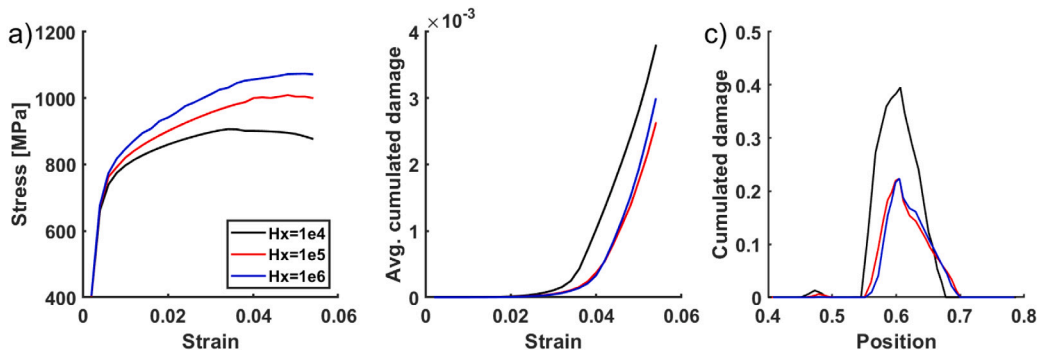


Fig. D.20. (a) Polycrystal hardening response for three H_x values, and (b) effective damage responses, and (c) line plot over a damage region at 5.5% of axial strain, using slip and damage regularization mode. Modulus A is set to 1.0 MPa mm^2 .

interactions. The stress–strain response in Fig. D.21a elucidates this phenomenon with the realization of stronger hardening rate of the polycrystal. The simulations were performed with regularization placed on both slip and damage. The hardening characteristics of higher value of $H_x = 10^5$ MPa increases the local stresses that trigger damage at an earlier stage than with $H_x = 10^4$ MPa. This observation is contrary to what is observed in Fig. 9 mainly because the stresses are elevated to a such extend that damage is triggered more and more by the influence of stress and not prior slip related softening of cleavage resistance. Parameter A can be used to evolve length-scale during deformation since it does not need remain constant (Dahlberg and Boåsen, 2019; Scherer et al., 2019; Chang et al., 2016). This alternative formulation allows to control the finite size of shear band thickness and therefore it could also be used to control damage in the shear band region.

As has become clear with single crystal simulations, the severity of damage is controlled with two main parameters after nucleation, the coupling parameter β and softening parameter H . Here, their meaning is further examined with polycrystalline structure. One physical interpretation for exercising slow or fast damage rate in the simulations is the control over the formation of nano-cracks and their extension to micro-cracks, which eventually is perceived as short-crack growth towards failure critical crack formation. Fig. D.22a, b present the effect of softening parameter H on overall softening behavior for a polycrystalline microstructure. A large parameter value promotes very rapid brittle-like damage growth soon after damage onset, similarly to single crystal cases. A decreasing value then oppositely reflects more ductile behavior. Coupling parameter β dictates how early damage develops after plastic slip concentration begin to form and eventually assists strain and damage localization due to two-way coupling effect of the parameter. High β value effectively decreases cleavage resistance at highly deformed zones in the first place, promoting rapid deterioration. Relative smooth softening curves are achievable whenever softening parameter H is chosen low.

Regularization of both slip and damage provides significant additional control on damage propagation. The curves feature small or large incubation softening periods after damage initiation before softening occurs on more detrimental slope. At increasing values of either or both β and H , the rapid softening following the incubation period begins to feature similar slopes than without dual-regularization. Whenever regularization is placed on slip alone, a damage biased flow begins to overtake after damage initiation irrespective of the value of β , supporting the observed behavior in Fig. 10.

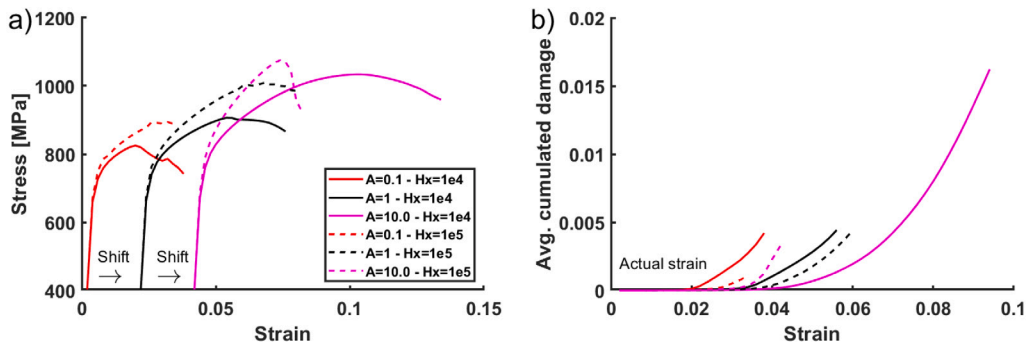


Fig. D.21. (a) Stress–strain curves for three higher order modulus and two penalty modulus values, and (b) average damage evolution in the microstructure for each simulation. Origin is shifted for different cases in the stress–strain plot for clarity.

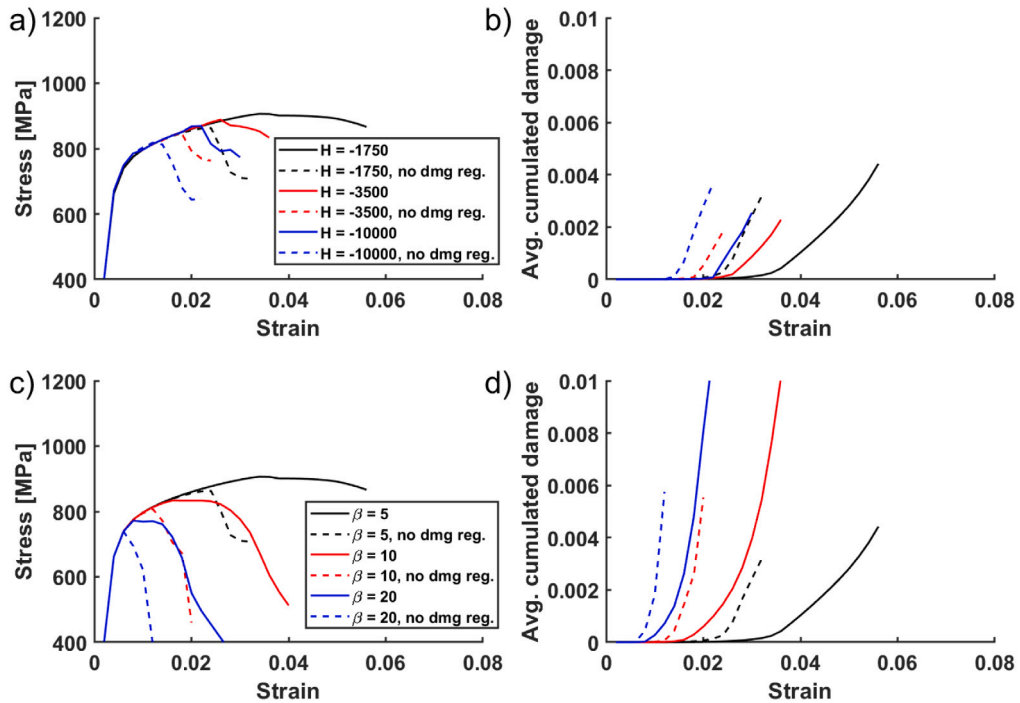


Fig. D.22. Effect of damage softening parameter H on (a) stress–strain behavior, (b) damage evolution with $\beta = 5.0$. Effect of plasticity–damage coupling parameter β on (a) stress–strain behavior and (b) damage evolution with $H = -1750$ MPa. Micromorphic parameters are $H_x = 10^5$ MPa and $A = 1.0$ MPa mm².

References

Abu Al-Rub, R., Ettehad, M., Palazotto, A., 2015. Microstructural modeling of dual phase steel using a higher-order gradient plasticity–damage model. *Int. J. Solid Struct.* 58, 178–189.

Acharya, A., Bassani, J., 2000. Lattice incompatibility and a gradient theory of crystal plasticity. *Acta Mater.* 47, 11597–11611.

Ashby, M., 1970. The deformation of plastically non-homogeneous materials. *Philos. Mag. J. Theoret. Exp. Appl. Phys.* 21 (170), 399–424.

Asik, E., Perdahcioglu, E., v.d. Boogaard, T., 2020. An RVE-based study of the effect of martensite banding on damage evolution in dual phase steels. *Materials* 13 (1795), 1–24.

Aslan, O., Cordero, N., Gaubert, A., Forest, S., 2011a. Micromorphic approach to single crystal plasticity and damage. *Int. J. Eng. Sci.* 49, 1311–1325.

Aslan, O., Quilici, S., Forest, S., 2011b. Numerical modeling of fatigue crack growth in single crystals based on microdamage theory. *Int. J. Damage Mech.* 20, 681–705.

Besson, J., Foerch, R., 1998. Object-oriented programming applied to the finite element method part I. general concepts. *Rev. Eur. Elém. Finis* 7 (5), 535–566.

Boeff, M., A., M., Hartmaier, A., 2014. Plastic deformation modelling of tempered martensite steel block structure by a nonlocal crystal plasticity model. *Theoret. Appl. Mech. Lett.* 4, 051007.

Boeff, M., Gutknecht, F., Engels, P., A., M., Hartmaier, A., 2015. Formulation of nonlocal damage models based on spectral methods for application to complex microstructures. *Eng. Fract. Mech.* 147, 373–387.

Brepols, T., Wulfinghoff, S., Reese, S., 2017. Gradient-extended two-surface damage-plasticity: Micromorphic formulation and numerical aspects. *Int. J. Plast.* 97, 64–106.

- Chang, H.-J., Cordero, N., Dépres, C., Fivel, M., Forest, S., 2016. Micromorphic crystal plasticity versus discrete dislocation dynamics analysis of multilayer pile-up hardening in a narrow channel. *Arch. Appl. Mech.* 86, 21–38.
- Chatterjee, A., Ghosh, A., Moitra, A., Bhaduri, A., Mitra, R., Chakrabarti, D., 2018. Role of hierarchical martensitic microstructure on localized deformation and fracture of 9cr-1mo steel under impact loading at different temperatures. *Int. J. Plast.* 104, 104–133.
- Cordero, N., Forest, S., Busso, E., 2013. Micromorphic modelling of grain size effects in metal polycrystals. *Ges. Angew. Math. Mech.* 36 (2), 186–202.
- Cordero, N., Gaubert, A., Forest, S., Busso, E.P., Gallerneau, F., Kruch, S., 2010. Size effects in generalised continuum crystal plasticity for two-phase laminates. *J. Mech. Phys. Solids* 58 (11), 1963–1994.
- Dahlberg, C.F., Boåsen, M., 2019. Evolution of the length scale in strain gradient plasticity. *Int. J. Plast.* 112, 220–241.
- Du, C., Hoefnagels, J., Vaes, R., Geers, M., 2016. Plasticity of lath martensite by sliding of substructure boundaries. *Scr. Mater.* 120, 37–40.
- Eringen, A., Suhubi, E., 1964. Nonlinear theory of simple microelastic solids. *Int. J. Eng. Sci.* 2, 189–203, 389–404.
- Fleck, N., Hutchinson, J., 1997. Strain gradient plasticity. *Adv. Appl. Mech.* 33, 296–361.
- Forest, S., 2008. Some links between cosserat, strain gradient crystal plasticity and the statistical theory of dislocations. *Phil. Mag.* 88 (30–32), 3549–3563.
- Forest, S., 2009. The micromorphic approach for gradient elasticity, viscoplasticity, and damage. *J. Eng. Mech.* 135 (3), 117–131.
- Forest, S., 2016. Nonlinear regularisation operators as derived from the micromorphic approach to gradient elasticity, viscoplasticity and damage. *Proc. R. Soc. A* 472, 20150755. <http://dx.doi.org/10.1098/rspa.2015.0755>.
- Forest, S., Sedláček, R., 2003. Plastic slip distribution in two-phase laminate microstructures: Dislocation-based vs. generalized-continuum approaches. *Phil. Mag.* 83, 245–276.
- Gurtin, M.E., 2002. A gradient theory of single-crystal viscoplasticity that accounts for geometrically necessary dislocations. *J. Mech. Phys. Solids* 50 (1), 5–32.
- Gurtin, M.E., 2004. A gradient theory of small-deformation isotropic plasticity that accounts for the Burgers vector and for dissipation due to plastic spin. *J. Mech. Phys. Solids* 52 (11), 2545–2568.
- Han, X., Besson, J., Forest, S., Tanguy, B., Bugat, S., 2013. A yield function for single crystals containing voids. *Int. J. Solids Struct.* 50 (14–15), 2115–2131.
- Hoc, T., Forest, S., 2001. Polycrystal modelling of IF-ti steel under complex loading path. *Int. J. Plast.* 17 (1), 65–85.
- Kaiser, T., Menzel, A., 2019. A dislocation density tensor-based crystal plasticity framework. *J. Mech. Phys. Solids* 131, 276–302. <http://dx.doi.org/10.1016/j.jmps.2019.05.019>.
- Kocks, U., Mecking, H., 2003. Physics and phenomenology of strain hardening: the FCC case. *Progr. Mater. Sci.* 48 (3), 171–273.
- Kwak, K., Mayama, T., Mine, Y., K., T., 2016. Anisotropy of strength and plasticity in lath martensite steel. *Mater. Sci. Eng. A* 674, 104–116.
- Kweon, S., 2016. A crystal-plasticity-based damage model incorporating material length-scale. *J. Eng. Mater. Technol.* 138 (3), 031002.
- Laukkanen, A., Uusikallio, S., Lindroos, M., Andersson, T., Porter, D., Komi, J., 2021. Micromechanics driven design of lean duplex steel microstructures for improved cleavage fracture toughness. *Eng. Fract. Mech.* 253, 107878.
- Li, D.-F., Barrett, R., O'Donoghue, P., Hyde, C., O'Dowd, N., Leen, S., 2016. Micromechanical finite element modelling of thermo-mechanical fatigue for P91 steels. *Int. J. Fatigue* 87, 192–202.
- Li, D.-F., Golden, B., O'Dowd, N., 2014. Multiscale modelling of mechanical response in a martensitic steel: A micromechanical and length-scale-dependent framework for precipitate hardening. *Acta Mater.* 80, 445–456.
- Li, M., Sun, F., Li, D.-F., O'Donoghue, P., Leen, S., O'Dowd, N., 2018. The effect of ferrite phases on the micromechanical response and crack initiation in the intercritical heat-affected zone of a welded 9Cr martensitic steel. *Fatigue Fract. Eng. Mater. Struct.* 41, 1245–1259.
- Lindroos, M., Laukkanen, A., Andersson, T., Vaara, J., Mantyla, A., Frondelius, T., 2019. Micromechanical modeling of short crack nucleation and growth in high cycle fatigue of martensitic microstructures. *Comput. Mater. Sci.* 170, 109185.
- Ling, C., Besson, J., Forest, S., Tanguy, B., Latourte, F., Bosso, E., 2016. An elastoviscoplastic model for porous single crystals at finite strains and its assessment based on unit cell simulations. *Int. J. Plast.* 84, 58–87.
- Ling, C., Forest, S., Besson, J., Tanguy, B., Latourte, F., 2018a. A reduced micromorphic single crystal plasticity model at finite deformations. Application to strain localization and void growth in ductile metals. *Int. J. Solids Struct.* 134, 43–69. <http://dx.doi.org/10.1016/j.ijsolstr.2017.10.013>.
- Ling, C., Forest, S., Besson, J., Tanguy, B., Latourte, F., 2018b. A reduced micromorphic single crystal plasticity model at finite deformations. Application to strain localization and void growth in ductile metals. *Int. J. Solids Struct.* 134, 143–169.
- Mareau, C., 2020. A non-local damage model for the fatigue behaviour of metallic polycrystals. *Phil. Mag.* 100, 955–981. <http://dx.doi.org/10.1080/14786435.2020.1713412>.
- Maresca, F., Kouznetsova, V., Geers, M., 2014. On the role of interlath retained austenite in the deformation of lath martensite. *Model. Simul. Mater. Sci. Eng.* 22, 045011.
- Maresca, F., Kouznetsova, V., Geers, M., 2016. Deformation behaviour of lath martensite in multi-phase steels. *Scr. Mater.* 110, 74–77.
- Mindlin, R., 1964. Micro-structure in linear elasticity. *Arch. Ration. Mech. Anal.* 16, 51–78.
- Monnet, G., Vincent, L., Gélébart, L., 2019. Multiscale modeling of crystal plasticity in reactor pressure vessel steels: Prediction of irradiation hardening. *J. Nucl. Mater.* 514, 128–138.
- Morito, S., Tanaka, H., Konishi, R., Furuhashi, T., Maki, T., 2003. The morphology and crystallography of lath martensite in Fe-C alloys. *Acta Mater.* 104, 1789–1799.
- Morsdorf, L., Jeannin, O., Barbier, D., Mitsuhashi, M., Raabe, D., Tazan, C., 2016. Multiple mechanisms of lath martensite plasticity. *Acta Mater.* 121, 202–214.
- Pineau, A., Forest, S., 2017. Effects of inclusions on the very high cycle fatigue behaviour of steels. *Fatigue Fract. Eng. Mater. Struct.* 9, 1694–1707.
- Pinomaa, T., Yaschuk, I., Lindroos, M., Andersson, T., Provatias, N., Laukkanen, A., 2019. Process-structure-properties-performance modeling for selective laser melting. *Metals* 9, 1138.
- Poh, L., Peerlings, R., Geers, M., Swaddiwudhipong, S., 2011. An implicit tensorial gradient plasticity model - formulation and comparison with a scalar gradient model. *Int. J. Solids Struct.* 48, 2595–2604.
- Rys, M., Forest, S., Petryk, H., 2020. A micromorphic crystal plasticity model with the gradient-enhanced incremental hardening law. *Int. J. Plast.* 128, 102655.
- Sabnis, P., Forest, S., Cormier, J., 2016. Microdamage modelling of crack initiation and propagation in FCC single crystals under complex loading conditions. *Comput. Methods Appl. Mech. Eng.* 312, 468–491.
- Schäfer, B., Sonnweber-Ribic, P., Hassan, H., Hartmaier, A., 2019. Micromechanical modelling of the influence of strain ratio on fatigue crack initiation in a martensitic steel - A comparison of different fatigue indicator parameters. *Materials* 12, 2852.
- Scherer, J.-M., Besson, J., Forest, S., Hure, J., Tanguy, B., 2019. Strain gradient crystal plasticity with evolving length scale: Application to voided irradiated materials. *Eur. J. Mech. A* 77, 103768.
- Scherer, J., Besson, J., Forest, S., Hure, J., Tanguy, B., 2021. A strain gradient plasticity model of porous single crystal ductile fracture. *J. Mech. Phys. Solids* 156, 104606. <http://dx.doi.org/10.1016/j.jmps.2021.104606>.
- Scherer, J.-M., Phalke, V., Besson, J., Forest, S., Hure, J., Tanguy, B., 2020. Lagrange multiplier based vs micromorphic gradient-enhanced rate-(in) dependent crystal plasticity modelling and simulation. *Comput. Methods Appl. Mech. Eng.* 372, 113426.
- Tazan, C., Hoefnagels, J., Diehl, M., Yan, D., Roters, F., Raabe, D., 2014. Strain localization and damage in dual phase steels investigated by coupled in-situ deformation experiments and crystal plasticity simulations. *Int. J. Plast.* 63, 198–210.
- Tu, X., Ray, S., 2020. A coupled crystal plasticity FEM and phase-field model for crack evolution in microstructures of 7000 series aluminum alloys. *Eng. Fract. Mech.* 230, 106970.

- Vincent, L., Libert, M., Marini, B., Rey, C., 2010. Towards a modelling of RPV steel brittle fracture using crystal plasticity computations on polycrystalline aggregates. *J. Nucl. Mater.* 406, 91–96.
- Wu, Q., Zikry, M., 2014. Microstructural modeling of crack nucleation and propagation in high strength martensitic steels. *Int. J. Solid Struct.* 51, 4345–4356.
- Wulfinghoff, S., Böhlke, T., 2012. Equivalent plastic strain gradient enhancement of single crystal plasticity: theory and numerics. *Proc. R. Soc. A* 468 (2145), 2682–2703.
- Z-set package, 2013. Non-linear material & structure analysis suite. www.zset-software.com.
- Zhang, Y., Lorentz, E., Besson, J., 2018. Ductile damage modelling with locking-free regularised GTN model. *Int. J. Numer. Methods Eng.* 113 (13), 1871–1903.
- Zhao, N., Roy, A., Wang, W., Zhao, L., Silberschmidt, V., 2019. Coupling crystal plasticity and continuum damage mechanics for creep assessment in cr-based power-plant steel. *Mech. Mater.* 130, 29–32.
- Zouaghi, A., Velay, V., Soveja, A., Pottier, T., Cheikh, M., Rézai-Aria, F., 2016. A multi-scale approach to investigate the nonlinear subsurface behavior and strain localization of X38CrMoV5-1 martensitic tool steel: Experiment and numerical analysis. *Int. J. Plast.* 87, 130–153.